Shape and Dimensions of Ripples

Jacobsen, Niels Gjøl; Fredsøe, Jørgen

Publication date:
2007

Document Version
Publisher's PDF, also known as Version of record

Shape and Dimensions of Ripples

Author:
Niels Gjøl Jacobsen

August 1st 2007

MEK, Technical University of Denmark
Kgs. Lyngby, Denmark

Contents

Nomenclature

Greek Characters

α	Closure coefficient in the k-ω-model
β	Closure coefficient in the k-ω-model
β	Coefficient in point distribution along the bed shape
β^*	Closure coefficient in the k-ω-model
δ_P	Penetration depth
ϵ	Dissipation of turbulent kinetic energy
ϵ	Upper boundary when evaluating I_U
ϕ_+	The phase lag between the free stream and the upstream seperation
ϕ_-	The phase lag between the free stream and the lee side seperation
Γ	The strength of the recirculation cell over the computational domain
Γ_0	The strength of the recirculation cell over the size of this cell
λ	Ripple length
μ	Gravity correction parameter
ν	Molecular kinematic viscosity
ν_T	Turbulent eddy viscosity
Ω	Vorticity
ω	Cyclic frequency
ω	Specific dissipation rate in the k-ω-model
ω_b	Boundary condition at the bed in the k-ω-model
Φ_B	Non-dimensional bed load transport

ρ	Density of water
σ	Closure coefficient in the k-ω-model
σ^*	Closure coefficient in the k-ω-model
τ_b	Bed shear stress
τ_{ij}	Reynolds stress tensor
θ	The Shields parameter due to skin friction
θ^*	The Shields parameter due to skin friction with gravity correction.

Roman Characters

a	Near bed amplitude of the oscillatory flow
A	The area of half the computational domain
$A(\delta_P)$	The area of the computational domain from the bed to the penetration depth
D	Height of the computational domain
d	The median grain diameter
f	The degree of rouding of the parabolic shaped bed form
f_w	Friction factor for wave motion
g	Acceleration due to gravity
h_0	Ripple height
$\mathbf{h}$	Parametric formulation of the ripple profile
$\tilde{h}_0$	Reduced height when smoothing the parabolic shape
h	The ripple profile
I_τ	Integral of the period averaged bed shear stress over half a ripple length
I_U	Integration of the horizontal velocity component over the horizontal
I_{Φ_B}	Bed load integrated over half the ripple profile
$I_{T/2}$	Integral of the bed shear stress over half a period and half the ripple length
$I_{T/2}$	Integral of the period averaged bed shear stress over half the ripple length

k	Turbulent kinetic energy
k_N	Nikuradse's roughness
k_N^+	Nikuradse's roughness non-dimensionlized by wall quantities
p	Pressure
q_B	Bed load transport
ΔQ_0	Threshold for the drift in the numerical model
ΔQ	Drift in the numerical model
r	Radius of the rounding of the parabolic shaped bed form
S	Parameter used to described the ripple profile
s	Relative density of sediment grains
S_R	Closure coefficient in the boundary condition for ω
T	Wave period
t	Time
U	Horizontal time averaged velocity component
u	Horizontal velocity component
U_f	The friction velocity
U_m	Maximum velocity of the near bed oscillatory motion
$U_{f,0}$	The maximum friction velocity on a flat bed
U_b	Horizontal component of the near bed flow
u'	Horizontal fluctuating velocity component
V	Vertical averaged velocity component
v	Vertical velocity component
v'	Vertical fluctuating velocity component
w_s	Sediment fall velocity
W	Magnitude of the velocity vector
x_S	Distance from the crest to stable point
Δy	The averaged horizontal resolution of the wall computational cells

y^+ Wall coordinate

y_0 The center of the smoothing

Definitions and Other Parameters

$\mathcal{N}_S$ Number of successive periods within the threshold ΔQ_0

$\mathcal{N}_T$ Number of time steps per wave period

$\mathcal{N}_x$ Number of computational cells in the x-direction

$\mathcal{N}_y$ Number of computational cells in the y-direction

Re_a The Reynolds number based on a and U_m

$\mathcal{S}_{91\%}$ The parabolic shaped bed form smoothed to 91% of the maximum slope

$\mathcal{S}_{93\%}$ The parabolic shaped bed form smoothed to 93% of the maximum slope

$\mathcal{S}_{97\%}$ The parabolic shaped bed form smoothed to 97% of the maximum slope

$\mathcal{S}_{100\%}$ The parabolic shaped bed form

$\mathcal{S}_1$ The cosine shaped bed form

$\mathcal{S}_2$ The higher order cosine shaped bed form

Preface

This thesis is part of the requirement for achieving my master degree in civil engineering from the Technical University of Denmark.

The work has been carried out at the department for Mechanical Engineering within the Coastal, Maritime and Structural Engineering Section under the supervision of Jørgen Fredsøe, David Fuhrman and B. Mutlu Sumer.

I would like to give thanks to my advisors for always being there to discuss results during the project period and to guide and limit me through this project. Further I would like to thank the other employees at the section and my co-students which made it an enjoyable place to work. Special thanks to Kasper Kærgaard for the many hours we discussed problems the last month of our master theses. Finally, thanks to family and friends which have supported me and shown interest in my progress throughout the entire period.

Acknowledgment: Many thanks to the Danish Center for Scientific Computing (DCSC) who made huge amounts of computational time available for me. My thesis would have suffered significantly, if this computational time had not been available.

August 1st 2007, Kgs. Lyngby

Niels Gjøl Jacobsen

Abstract

In this work, the flow and bed load transport over ripple profiles under the influence of oscillatory will be investigated. The investigation is made through a parametric study, where the bed shape and the ripple steepness are varied. For the sediment transport, the Shields parameter relative to the critical one is varied in the range 1.31-3.45.

A detailed flow description in terms of phase resolved quantities and period averaged quantities are given. The former are phase lag between the free stream flow and the separation and a description of the lee side vortices behind vortex ripples. The latter are the recirculation zone and its penetration into the main flow. This will be compared to the period averaged bed shear stress.

An analysis of the bed load transport, both as a transport capacity in the phase resolved space and an analysis of possible stable ripples is conducted. This leads to some stable ripples and the general conclusion is that sharp crested ripples is thought unlikely to become stable under oscillatory flow due to the large increase in bed shear stresses because of the rapid contraction of the flow around the crest.

Further, a dynamically moving ripple crest is investigated. The key focus is to investigate how a perturbation on top of the ripple influences the flow. It will be seen that both the shape and the velocity of the crest are affecting the period averaged flow globally.

Abstract in Danish

I denne afhandling vil strømning og bundtransport over bølgegenererede ribber blive undersøgt. Undersøgelsen baserer sig på et parametrisk studie, hvor det er ribbeformen og stejlheden af denne, som varieres. Med henhold på bundtransporten, så bliver Shields parametren i forhold til den kritiske værdi varieret i intervallet 1.31-3.45.

Der vil blive givet en detaljeret strømningsbeskrivelse både med henblik på en faseopløst beskrivelse samt en periodmidlet beskrivelse. Den første inkluderer faseforskellen mellem seperation og den frie strømning samt en beskrivelse af hvivlerne nedstrøms ribbetoppen. Den periodmidlede beskrivelse behandler recirkulationszonen og dennes indflydelse på den ydre strømning. Disse resultater vil blive sammenholdt med den periodemidlede bundforskydningsspænding.

En analyse af bundtransporten er udført med henblik på transportkapaciteterne samt, om der er mulige stabile ribbeformer. Denne analyse udpeger nogle stabile former, og den generelle konklusion er, at ribber med en spids top bliver betragtet som usandsynlige som stabile former under bølgepåvirkning grundet forøgelsen i bundforskydningsspændingerne. Denne forøgelse optræder på grund af den kraftige kontraktion ved ribbetoppen.

Endvidere er en dynamisk ribbetop undersøgt. Formålet med dette er at undersøge, hvordan en perturbation som bevæger sig inden for en bølgeperiode påvirker strømningen. Det vil blive vist, at både formen og hastigheden af en sådan perturbation påvirker det periodemidlede strømningsfelt globalt.

Chapter 1

Introduction

In this work, the goal is to determine the shape of ripples subject to oscillatory motion. Further a detailed flow description due to the interaction between ripple profile and water will be carried out. The motivation is to make a first step toward the shape of ripples under combined waves and current or waves including streaming effects. Knowing the equilibrium shape, the period averaged sediment transport can be estimated more accurately. This type of sediment transport is typically linked to the cross shore sediment transport in coastal zones, thus estimates of coastal evolution can attribute from a more detailed description.

Many experimental works have been made to described the evolution of the ripple profiles and the flow over these starting with Bagnold (1946), where he oscillates a tray covered with sand in otherwise still water. This method is doubtful as the shape of the ripples will be influenced by the grain inertia, thus ripple profiles in these experiments should be expected to be less steep than under the same conditions achieved by oscillating the water. Based on these experiments, the distinction between rolling grain ripples and vortex ripples is introduced.

The theoretical work by Fredsøe and Hedegaard (1983) uses a simple back-ward facing step approximation with a constant shear stress outside the separation zone. This lead to three theoretical shapes of ripples where bed load dominates. Two of these shapes are stable. Further, from the work of Hedegaard (1985) a simple relation of the ripple length was found, namely $\lambda = 1.2a$, with λ being the ripple length and a the orbital amplitude of the near bed flow. The present work will be limited to this relation.

Further the theoretical work by Andersen (1999) made use of phase resolved morphological updating of the ripple profile. One of his findings was that the sediment and flow quantities was qualitatively the same averaged over one wave period when comparing live and rigid ripple profiles. This conclusion encouraged the present analysis using period averaged quantities.

The present work will try to reach the equilibrium profile through an inte-

grated formulation, i.e. in terms of the period averaged sediment transport. This will be done in a pure oscillatory flow and at first only bedload will be considered, thus the Shields parameter will be kept close to the critical value on a flat bed. The cloud of sediment ejected into the flow at the crest of the ripple, e.g. as discussed in Andersen (1999), will be ignored. This is valid since the ratio between the sediment fall velocity and the amplitude of the outer flow velocity, w_s/U_m, will be large.

As a first approximation, the flow will be that of an oscillator, thus there will be no streaming effects on a flat bed, hence the bed profile will throughout this work be perfectly symmetric. Further no percolation is taken into the description.

1.1 Physical Processes

When a flat bed subject to oscillatory motion is perturbed, two kinds of ripples can be generated. These are termed "rolling grain ripples" and "vortex ripples" respectively, see figure 1.1. The former is present up to $h_0/\lambda < 0.1$ and the latter in the range $0.1 < h_0/\lambda < 0.25$, where λ is the ripple length and h_0 the trough-to-crest height, see Sleath (1984).

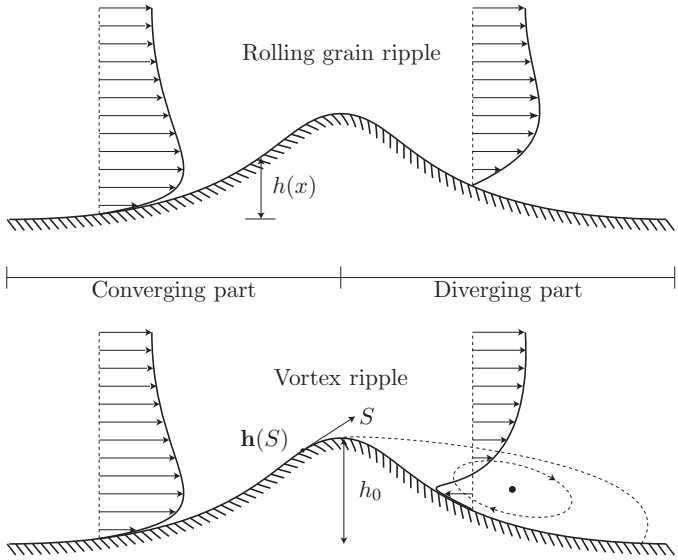

Figure 1.1: *Sketch of the difference between rolling grain ripple and vortex ripples. Two ways of representing the ripple profile is shown, namely in cartesian coordinates and using a parametric formulation with the parameter S.*

Rolling grain ripples are characterized by a perturbation where separation does not occur on the lee side of the ripple whereas separation does

occur in the case of vortex ripples. Separation is the one occurring due to expansion of the cross section and not the one due to flow reversal each half period. The latter type of separation will be termed "separation due to flow reversal".

These two types of ripples have some common physical features. First these feature will be mentioned in overview and secondly the cause and effect will be discussed in greater detail.

1. At the end of each half wave period there will be ejection of vortices into the main part of the flow. This vortex will gain larger and larger distances to the bed while being dissipated.

2. A non-zero period averaged bed shear stress will be directed toward the crest of the perturbation. The non-zero bed shear stress will drive a streaming effect.

3. There will be a period averaged non-zero sediment transport directed toward the crest.

These features will now be discussed in details and differences between rolling grain ripples and vortex ripples will be discussed, if such differences exist.

ad. 1. Due to reversal of the outer flow each half wave period, the vortex generated in the previous half period is ejected into the main flow. This vortex is generated in two different ways and due to two different mechanisms in the case of either rolling grain ripples or vortex ripples. In the case of the former it is generated at the point of flow reversal in the boundary layer and in the case of the latter it is generated as early as at the point where the vortex in the previous half period is ejected into the main flow. The mechanisms will be discussed later in the work, as it is one of the general findings.
After the ejection, the vortex moves up and down following the flow, but the general trend is that the vortex moves away from the bed, also reported Bagnold (1946) in his rigid bed experiment. This movement continues until the vortex is dissipated completely, thus a penetration depth into the main flow can be found. The variation of the penetration depth with bed shape and steepness is discussed in section 3.3.2.

ad. 2. In Sleath (1984) an analytical solution of the laminar oscillatory flow over a perturbed bed was given. This showed that to higher order, the solution yields time independent results, which have the same characteristics as the streaming over ripples, namely flow toward the crest at the bed, and flow toward the trough some distance from the bed, see figure 1.2 for a schematic presentation

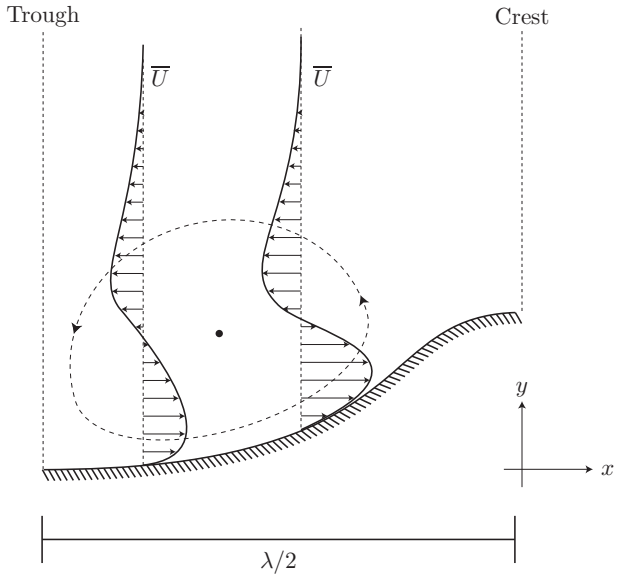

Figure 1.2: *Sketch of the recirculation cell over half a ripple length.*

In the more general case, the presence of such a recirculation zone can be argued based on the near bed behaviour of the flow. Engelund and Fredsøe (1974) argues that in order to get instability of a perturbed bed in the case of dunes dominated by bed load, it is not sufficient to calculate the bed shear stress from the local depth, the average velocity and a constant friction factor. An effect of convergence and divergence of the flow has to be taken into consideration, see figure 1.1, thus the friction is modified by a local slope correction yielding increased bed shear stress on the converging part and decreased on the diverging part. This analysis of the flow can be carried over to the case of oscillatory flow. Since the bed shear stress in the case of Engelund and Fredsøe (1974) is asymmetric around the crest, the period averaged bed shear stress will become non-zero in the case of waves. This non-zero bed shear stress will be directed toward the crest, based on the increase on the converging side. Finally this bed shear stress drives a period averaged flow toward the crest at the bed and from continuity reasons, this flow must be in the opposite direction some distance from the bed.

In the following the general cause and effect will be discussed, since a different point of view on the recirculation zone leads to a different cause to the driving mechanism.

ad. 3. As discussed by Sleath (1984), the recirculation is the mechanism behind the increasing height of the ripple, as there will be a net sediment

transport toward the crest, as long as the induced bed shear stresses are sufficiently large. This transport will then stop, when the steepness of the ripple exceeds the steepness where gravity become dominant. This ending of build up of ripples can be illustrated by the results in Bagnold (1946) where a stable rolling grain ripple was found when it reached a certain height.

A couple of things should be kept in mind regarding the flow, when choosing an appropriate numerical flow solver. These are that the flow is over a rough surface, thus the model should be capable of treating rough boundaries. The flow is not always wall bounded due to the adverse pressure gradient coming from the free stream flow and the adverse pressure gradient induced due to the expansion of the cross sectional area on the lee side of the crest. Thus the numerical model should be capable of treating adverse pressure gradients and separated flows as well. The numerical model will be discussed in section 2.1.

1.2 Dimensionless Quantities

This section is mainly inspired by the work of Andersen (1999). The flow over ripples has been found to rely on several different non-dimensional parameters. For the ripple-flow interaction

$$\frac{\lambda}{a} \quad , \quad \frac{h_0}{\lambda} \tag{1.1}$$

are of significant importance and such values as

$$\frac{k_N}{a} \quad , \quad \frac{D}{a} \quad , \quad Re_a = \frac{aU_m}{\nu} \tag{1.2}$$

are of minor importance. λ is the ripple length, a is the near bed amplitude, h_0 is the height of the ripple, $k_N = 2.5d$ is the Nikuradses roughness, where d is the grain median diameter, D is the height of the computational domain and Re_a is the Reynolds number.

Regarding the sediment transport the following parameters are of importance

$$\theta = \frac{U_f^2}{(s-1)gd} \quad , \quad \frac{w_s}{U_m} \quad , \quad s \tag{1.3}$$

where the last is of less importance compared to the other. s is the relative density of the sediment to water. θ is the Shields parameter and w_s is the fall velocity of the individual grains, which is calculated as outlined in Fredsøe and Deigaard (1995).

In the present study the dependence of the ripple steepness, h_0/λ, and θ will be investigated with respect to flow properties and bed load sediment

transport. w_s is changed as a consequence of changing θ and demanding constant roughness, a/k_N. The effect of the change in w_s is not investigated as it is kept so large, that it is assumed that suspended sediment transport is neglectable.

Chapter 2

Model Description

In this chapter the numerical model is described in terms of the flow solver and the sediment transport formulations. Regarding the sediment transport it will only concern bedload, since suspended sediment transport is neglected in the present analysis. The numerical model is verified against the measurements by Jensen *et al.* (1989). Further an analysis of the necessary parameters needed to obtain a grid independent solution is discussed and a grid configuration is chosen.

2.1 Mathematical Formulation of Flow Solver

In section 1.1 it was discussed that adverse pressure gradients are present in the flow. In Wilcox (1993) he states that a k-ω-model succeeds in modeling flow with adverse pressure gradients whereas k-ϵ-models are not capable of doing so. Further it is stated by Patel and Yoon (1995) that the tested k-ϵ-model underestimates the bed shear stress even on a flat rough bed, whereas the k-ω-model estimates the bed shear stress within a few percent of the Moody-diagrams.

Based on these arguments the k-ω-model by Wilcox (1994) will be used in this study. The model is based on the following mathematical formulation, namely the continuity equation

$$\frac{\partial u_i}{\partial x_i} = 0 \tag{2.1}$$

and the Navier-Stokes equations

$$\frac{\partial u_i}{\partial t} + u_j \frac{\partial u_i}{\partial x_j} = -\frac{\partial p}{\partial x_i} + \nu \frac{\partial}{\partial x_j}\left(\frac{\partial u_i}{\partial x_j} + \frac{\partial u_j}{\partial x_i}\right) \quad , \tag{2.2}$$

where u_i are the velocity components, x_i are the spatial coordinates, t is the time, p is the pressure and ν is the molecular kinematic viscosity. The

density, ρ, is left out as incompressible flows are considered. The velocity components are written as a combination of time averaged velocities and instantaneous velocity fluctuations

$$u_i = U_i + u_i' \tag{2.3}$$

with U_i being the time averaged component and u_i' the fluctuating part. Time averaging (2.1) and (2.2) becomes

$$\frac{\partial U_i}{\partial x_i} = 0 \tag{2.4}$$

$$\frac{\partial U_i}{\partial t} + U_j \frac{\partial U_i}{\partial x_j} = -\frac{\partial p}{\partial x_i} + \frac{\partial}{\partial x_j}\left[\nu\left(\frac{\partial U_i}{\partial x_j} + \frac{\partial U_j}{\partial x_i}\right) + \frac{\tau_{ij}}{\rho}\right] \quad . \tag{2.5}$$

The latter equations are called the Reynolds Averaged Navier-Stokes equations. τ_{ij} is the Reynolds stress tensor, which expresses the additional shear stresses due to momentum transfer from the turbulent fluctuations. This quantity is expressed in terms of the eddy viscosity concept by

$$\frac{\tau_{ij}}{\rho} = \nu_T\left(\frac{\partial U_i}{\partial x_j} + \frac{\partial U_j}{\partial x_i}\right) - \frac{2}{3}k\delta_{ij} \tag{2.6}$$

where δ_{ij} is the Kronecker delta and k is the turbulent kinetic energy

$$k = \frac{1}{2}\overline{u_i'^2} \quad . \tag{2.7}$$

The overbar denotes time averaging.

The equations adopted to close the system are taken from Wilcox (1994) with a transport equation for the turbulent kinetic energy

$$\frac{\partial k}{\partial t} + U_j \frac{\partial k}{\partial x_j} = \frac{\tau_{ij}}{\rho}\frac{\partial U_i}{\partial x_j} - \beta^* k\omega + \frac{\partial}{\partial x_j}\left[(\nu + \sigma^*\nu_T)\frac{\partial k}{\partial x_j}\right] \tag{2.8}$$

and a transport equations for the specific dissipation rate, ω,

$$\frac{\partial \omega}{\partial t} + U_j \frac{\partial \omega}{\partial x_j} = \alpha\frac{\omega}{k}\frac{\tau_{ij}}{\rho}\frac{\partial U_i}{\partial x_j} - \beta\omega^2 + \frac{\partial}{\partial x_j}\left[(\nu + \sigma\nu_T)\frac{\partial \omega}{\partial x_j}\right] \tag{2.9}$$

The coefficients in these two equations are closure coefficients which takes the values given in table 2.1.

The terms in equations (2.8) and (2.9) is on the left hand side temporal change and advection of k and ω respectively. On the right hand side the terms are production, dissipation and diffusion of k and ω respectively. The diffusion is a combination of molecular and turbulent diffusion. The presence of the molecular kinematic viscosity allows the model to describe the viscous

Table 2.1: *Closure coefficients for the k-ω-equations given in* (2.8) *and* (2.9).

α	β	β^*	σ	σ^*
5/9	3/40	9/100	1/2	1/2

sublayer without the use of wall functions which the k-ϵ-models are forced to use. This freedom allows the k-ω-model to solve for significantly more complex flows. The boundary condition for ω includes the surface roughness.

The final closure equation relates k and ω to the eddy viscosity by

$$\nu_T = \frac{k}{\omega} \quad . \tag{2.10}$$

Further the dissipation of turbulent kinetic energy, ϵ, can be expressed as

$$\epsilon = \beta^* \omega k \tag{2.11}$$

Special attention has to be given the continuity equation, (2.4), since it should be used to solve for the pressure, p, but the pressure is not a variable. Instead the continuity equation is applied onto the momentum equations, i.e. the divergence of the momentum equations are derived. This leads to a Poisson equation for p which is solved (see Tjerry, 1995, for details on the numerical treatment).

The described set of equations have been implemented in a research code called Dune2D. The core of the model has been developed by Tjerry (1995) whereas the k-ω-model has been implemented on a later stage.

2.1.1 Boundary Conditions

In this section the applied boundary conditions are described, see figure 2.1. At the upper boundary a symmetry condition is set, i.e. the vertical derivatives of all quantities have to be zero.

On the vertical boundaries a periodicity condition has been applied, which results in solving for an infinite number of ripples.

The bed boundary condition is somewhat more complex as a value, ω_b, needs to be pre-described to ω. The routine to describe the rate of dissipation is adopted by Wilcox (1994) in which

$$\omega_b = \frac{U_f^2}{\nu} S_R \tag{2.12}$$

at the bed, where U_f is the friction velocity defined by

$$U_f^2 = \frac{\tau_b}{\rho} \tag{2.13}$$

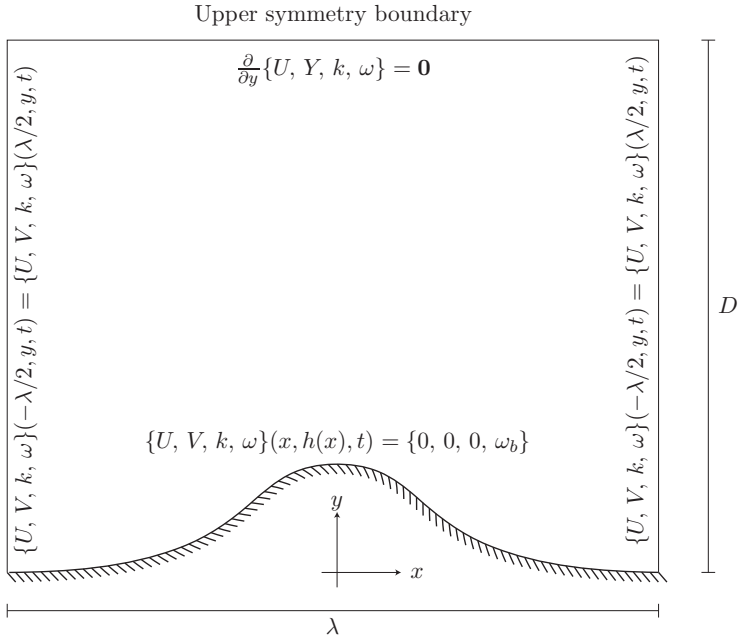

Figure 2.1: *Sketch of the boundary conditions in the computational domain.*

with τ_b being the bed shear stress. The quantity S_R is a function of the non-dimensional bed roughness, $k_N^+ = k_N U_f/\nu$, where k_N is the Nikuradse' roughness, $k_N = 2.5d$, and d is the median grain diameter. The dependency is given as

$$S_R = \begin{cases} (50/k_N^+)^2 & \text{for} \quad k_N^+ < 25 \\ 100/k_N^+ & \text{for} \quad k_N^+ \geq 25 \end{cases} \tag{2.14}$$

Patel and Yoon (1995) showed in their work that (2.14) on a flat bed is valid up to at least $k_N^+ = 4000$.

The velocity components, U_i, are set with a no-slip condition and the turbulent kinetic energy, k, is 0 at the bed.

The Poisson equation for the pressure is solved with homogeneous Neumann conditions on all boundaries.

2.1.2 Verification of the Flow Solver

The model will be verified against the experimental data by Jensen *et al.* (1989). The compared quantities are the bed shear stress as a function of time and the velocity profile for $\omega t = 90°$, where ω is the cyclic frequency, $2\pi/T$, with T being the wave period.

Figure 2.2 shows the comparison between the measured and calculated friction velocity, U_f, at different phases. The comparison shows an excellent

prediction by the numerical model both in terms of the magnitude of the friction velocity and the phase lag between the free stream flow and the bed shear stress.

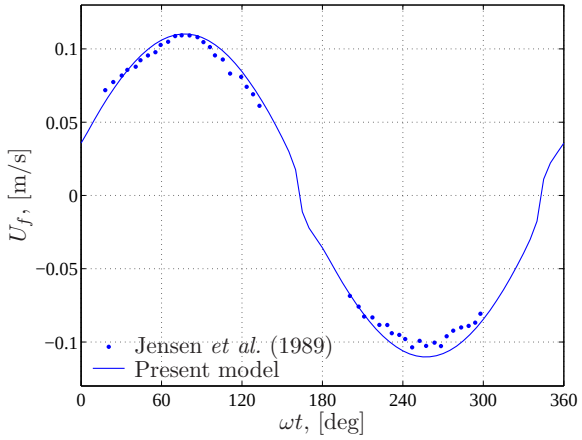

Figure 2.2: *Comparison between the present model and the experimental investigation by Jensen* et al. *(1989). The data points are taken from their figure 7.*

In figure 2.3 a comparison between the velocity profiles over the vertical for $\omega t = 90°$ is seen. In the figure the horizontal velocities are averaged with the instantaneous maximum velocity. As seen, there is a good prediction of the shape of the velocity profile.

2.1.3 Convergence of Waves

The numerical model generates an artificial drift, ΔQ, because the initial conditions are defined by setting all quantities to zero. This drift has an extremely slow convergence, thus the calculation time with pure waves is huge. Therefor another approach is needed.

It was realized that inducing a small pressure gradient, constant within one wave period, and changing it each period would make the convergence significantly faster. The method is the PID-control described in Andersen (1999).

This method is oscillatory in nature when approaching the correct solution, see sketch in figure 2.4, thus to avoid choosing the first zero crossing, which is not the desired solution, a demand for a number of successive occurrences, $\mathcal{N}_S$, within a threshold, ΔQ_0, is set. For the rest of this work $\mathcal{N}_S = 10$. The same procedure is working for combined waves and current.

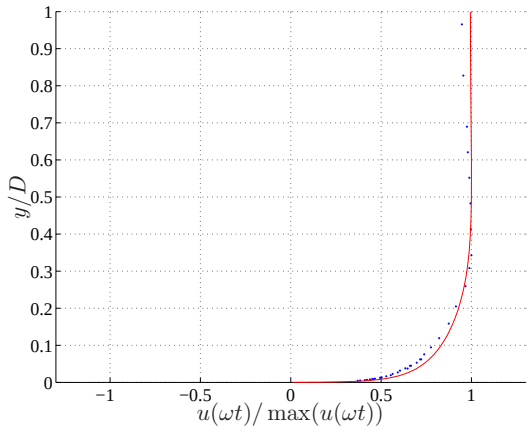

Figure 2.3: *Comparison between measured velocity profiles from Jensen* et al. *(1989) and the ones calculated by the present model for* $\omega t = 90°$. *The data is taken from their test 13.* D *is half the height of the oscillatory tunnel.*

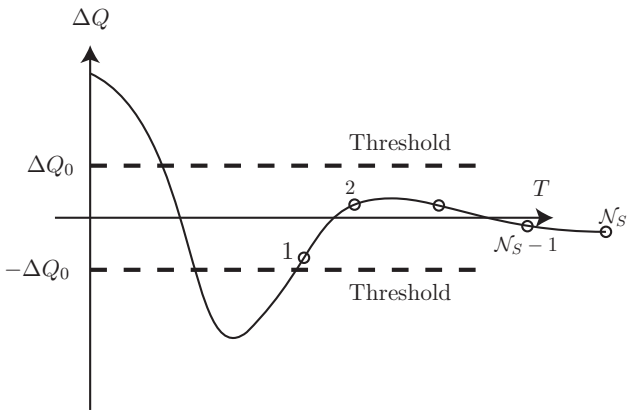

Figure 2.4: *Sketch of the oscillatory behaviour of the PID-control, where* ΔQ *is the drift in the system and* ΔQ_0 *is the threshold for the drift.*

2.1.4 Grid Generation

The grid for the numerical calculations is curvilinear and is generated using a hyperbolic grid generator, see Tjerry (1995). The method allows clustering of the grid points at the bed to allow better prediction of the bed shear stress. An example of a grid can be seen in figure 2.5.

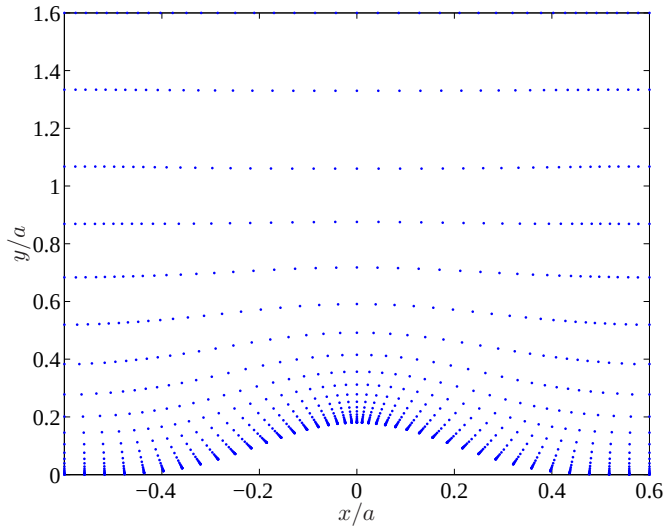

Figure 2.5: *Example of a grid generated using a hyperbolic grid generator with clustering of the points at the bed. The size of the grid is* $\mathcal{N}_x \times \mathcal{N}_y = 40 \times 30$.

2.1.5 Non-Dimensionality of the Model

The numerical model is made in terms of non-dimensional equations, where the equations have been made non-dimensional with appropriate length and velocity scales. In the present work U_m and a has been chosen to be the characteristic scales, thus all results in the following will be given in terms of non-dimensional results using these as characteristic scales.

Recall that the mass scale is indirectly chosen to be ρ, but it is not present in the model formulation due to incompressibility.

2.1.6 New Mathematical Formulation

It should be noted that the used model is based on Wilcox (1994), but research has been conducted in the recent years. In Wilcox (2006) the recommended model has been modified in terms of the ω-equation which has been added a cross-diffusion term between k and ω, the closure coefficients have been changed and the wall boundary condition for ω has been modified. The new model treats wall bounded flows as good as the model from Wilcox

(1994) which includes backward facing step type of flows, but for such flows as free shear flow, the model is improved. The present work with ripples is a combination of these two as the separation behind the ripple resembles the backward facing step, and the shedding of vortices every half wave period induces free shear. There has not been used time on implementing the new model.

2.2 Bedload Transport

When water flows over a bed consisting of loose grains, the grains will begin to move if the bed shear stress becomes larger than the retarding forces on the sediment. In the case of a flat bed and cohesive-less sediment this retarding force is the inter-granular friction.

The force balance between the destabilizing and retarding forces, see Fredsøe and Deigaard (1995), is expressed in terms of the Shields parameter due to skin friction

$$\theta = \frac{U_f^2}{(s-1)gd} \tag{2.15}$$

where U_f is the friction velocity, s is the relative density of the sediment compared to water, g is the acceleration due to gravity and d is the median grain diameter. The critical value of θ is found to vary with $Re_d = U_f d/\nu$, but only slightly, thus the critical value is throughout this work kept constant at $\theta_c = 0.05$.

In the present study the sediment transport will take place on sloping beds, where the influence of gravity will either increase or decrease the stability depending on the slope compared to the flow direction. This has resulted in a modification to include sloping beds, see Fredsøe (1974), namely

$$\theta^* = \frac{U_f^2}{(s-1)gd} - \mu \frac{\partial h(x)}{\partial x} \tag{2.16}$$

where μ takes the value 0.1.

The adopted transport formulae is the Meyer-Peter and Müller formulae including the above slope correction, see Fredsøe (1974), which looks like

$$\Phi_B = \frac{q_B}{\sqrt{(s-1)gd^3}} = 8(\theta^* - \theta_c)^{3/2} \tag{2.17}$$

This is a local sediment transport formulation which only take the mean flow quantities into considerations and not the level of turbulence. Regarding the influence of turbulence, this has been investigated recently by Sumer *et al.* (2003) and there is a clear correlation. This means that at the reattachment point of the vortex on the lee side the bed shear stress become zero in terms of averaged quantities, but due to turbulence there can be sediment transport. This feature is not captured.

2.3 Analysis of Grid Independence

In order to get consistent results, it is necessary to investigate whether it is possible to obtain grid independent results, i.e. that a small change in the grid does not change the results. Even though it sounds easy and objective, the choice of an "independent" grid is a trade-off between the desired accuracy and the available computational time.

The grid quantities, which have been identified to be of importance in the present work, are the resolution at the bed, since the bed shear stress is calculated directly based on the velocity gradient evaluated in the computational cell next to the bed.

Further the height of the domain is important because a too low domain results in lid generated effects, due to interaction between the ripple and the lid.

The number of computational cells in the x and y directions is of importance. The number of cells are referred to as $\mathcal{N}_x$ and $\mathcal{N}_y$ respectively. In the work by Andersen (1999) the resolution at the crest was investigated as well, namely the quantity $\Delta x/a$, but in the present work this has been avoided by investigating the necessary value of $\mathcal{N}_x$ and using the same distribution of the points along the bed throughout the work. The distribution cluster the points at the crest, since it is expected that a larger number of points is needed to describe the flow separation accurately. The distribution is given as

$$\frac{x}{a} = \frac{\lambda}{2a}\left[\frac{\sin(\beta N)}{\sin(\beta)} - 1\right] \tag{2.18}$$

where

$$\beta = \frac{9}{10}\frac{\pi}{2(\mathcal{N}_x/2+1)} \quad \text{and} \quad N = 0, 1, \ldots, \frac{\mathcal{N}_x}{2} \tag{2.19}$$

This gives a distribution of points along half a ripple length. This procedure needs to be reconsidered if combined waves and current is investigated, since that kind of forcing results in an asymmetric ripple profile, e.g. seen in Gray *et al.* (1991).

Finally the dependency on the number of time steps per wave period, $\mathcal{N}_T$, has been investigated for the chosen grid configuration.

The independence analysis uses a parabolic bed shape, see equation (3.3), with the steepness $h_0/\lambda = 0.167$ and $\lambda/a = 1.2$, where h_0 is the trough-to-crest height, λ is the ripple length and a is the near bed amplitude of the oscillatory motion.

From this point on, period averaged quantities will be given with an overbar, e.g.

$$\overline{U} = \frac{1}{T}\int_0^T U \mathrm{d}t \tag{2.20}$$

which is the period averaged horizontal velocity.

2.3.1 Bed Resolution

The bed resolution is described in terms of the non-dimensional wall coordinate

$$y^+ = \frac{\Delta y U_{f,0}}{\nu} \tag{2.21}$$

where Δy is the averaged height of the computational cells along the bed shape, $U_{f,0}$ is the friction velocity on a flat bed, which is determined from the empirical relation

$$U_{f,0}^2 = \frac{\tau_b}{\rho} = \frac{1}{2} f_w U_m^2 \quad , \quad f_w = 0.04 \left(\frac{a}{k_N} \right)^{-1/4} \quad \text{for} \quad \frac{a}{k_N} > 50 \tag{2.22}$$

(see Fredsøe and Deigaard, 1995) and ν is the kinematic viscosity. The flat bed property has been chosen since the actual friction velocity is not known in advance, thus it is more convenient to work with flat bed quantities.

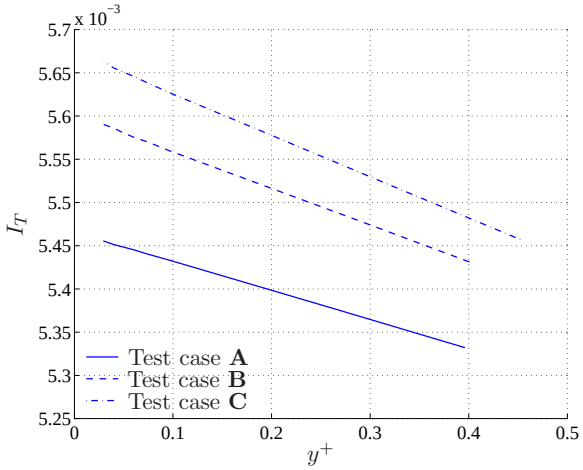

Figure 2.6: *I_T as a function of y^+ for three test cases,* **A**, **B**, *and* **C**, *see table 3.1. Other quantities are $\mathcal{N}_T = 1750$, $\mathcal{N}_x \times \mathcal{N}_y = 50 \times 50$.*

The convergence of the flow has been investigated in terms of

$$I_T = \frac{1}{\int_0^{1/2} \|\mathbf{h}'(S)\| \mathrm{d}S} \int_0^{1/2} \overline{\tau}_b \|\mathbf{h}'(S)\| \mathrm{d}S \tag{2.23}$$

where S is a coordinate following the ripple profile and the whole profile is given for the interval $S \in [0; 1]$, i.e. the integral is evaluated for the first

half part of the ripple. The entire profile is not usable, as I_T would become zero.

Considering the convergence of I_T as a function of y^+, see figure 2.6, it is seen that convergence has not been achieved for as small values of $y^+ = 0.03$. Decreasing y^+ below $\mathcal{O}(0.1)$ increases the necessary time steps significantly, thus $y^+ = \mathcal{O}(0.1)$ has been chosen to be used throughout the report. This choice induces errors in the order of magnitude of 1% in I_T, if the linear trend in figure 2.6 can be extrapolated to $y^+ = 0$. Wilcox (1994) reports that $y^+ < 1$ has to be used to obtain reasonable results.

2.3.2 Height of the Domain

The height of the domain has to be investigated to avoid effects on the flow from the upper boundary, i.e. it has to be investigated how far away the lid should be for I_T and

$$I_{T/2} = \frac{1}{\int_0^{1/2} \|\mathbf{h}'(S)\| dS} \int_0^{1/2} \frac{2}{T} \int_0^{T/2} \tau_b \|\mathbf{h}'(S)\| \mathrm{d}t \, \mathrm{d}S \tag{2.24}$$

to converge. $I_{T/2}$ expresses the bed shear stress over a half wave period on the upstream side of the crest. This integral is used in addition to I_T, since the convergence on the two sides of the crest for half a wave period differs, thus the combination of I_T and $I_{T/2}$ covers this.

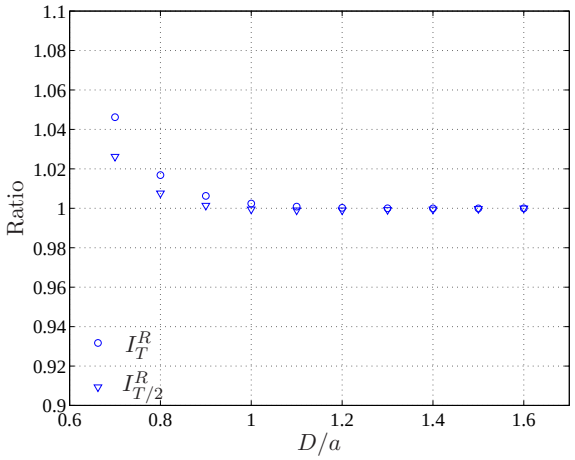

Figure 2.7: *Convergence analysis of the height of the computational domain, D/a, where D is the height of the domain and a the amplitude of the motion at the bed. $\mathcal{N}_T = 1750$, $\mathcal{N}_x \times \mathcal{N}_y = 50 \times 50$ and $y^+ = 0.08$. The superscript R means that the results are relative to the corresponding ones found for $D/a = 1.6$.*

Based on the results in figure 2.7, the height $D/a = 1.6$ has been chosen.

As help to future users, it is noted that the upper boundary in Dune2D is always at $y/\ell = 1$ in the grid generator, where ℓ is the characteristic length scale. A higher domain is thus generated by shifting the bed shape downward.

2.3.3 Grid Dimensions

When analyzing the necessary number of grid cells in the horizontal and vertical directions, $\mathcal{N}_x$ and $\mathcal{N}_y$ respectively, a two-dimensional feature has been used to analyse the convergence. This feature is

$$\Gamma A = \int_A \overline{\Omega} \mathrm{d}A \tag{2.25}$$

where Ω is the vorticity and A is half the area of the computational domain, namely

$$A = \left[-\frac{\lambda}{2a}; 0 \right] \times \left[\frac{h(x)}{a}; \frac{D}{a} \right] \tag{2.26}$$

This quantity expresses the strength of the recirculation cell which was discussed in section 1.1.

As figure 2.8 reveals, the results lie within a few percent, but it is not possible to point out one independent grid configuration. The main focus in this work is on the bed load and the two dimensionality, e.g. Γ, is secondary, thus for the rigid bed analysis, see chapters 3, the grid configuration $\mathcal{N}_x \times \mathcal{N}_y = 70 \times 40$ was chosen initially. This gave extremely bad convergence properties, thus simply to obtain results a grid configuration with $\mathcal{N}_x \times \mathcal{N}_y = 50 \times 40$ was adopted.

2.3.4 Independence of $\mathcal{N}_T$

The time stepping scheme is of first order, thus the number of time steps is of substantial importance. In figure 2.9 runs on a 50×40 grid for varying $\mathcal{N}_T$ are analysed. This analysis shows that the results converge for increasing $\mathcal{N}_T$, as expected. The analysis has been carried out for both test case **A** and **D**, see table 3.1, and no Reynolds dependence was found.

Based on this figure, $\mathcal{N}_T = 1000$ has been chosen for the rigid bed analysis. It results in errors in the order of magnitude of 2%, which has been accepted over the linearly increasing computational time when increasing $\mathcal{N}_T$.

2.3.5 Comment Regarding the Point Distribution

It is realized that the method for distributing the points along the bed induces peaks in the bed shear stress at the "crest" even if the steepness

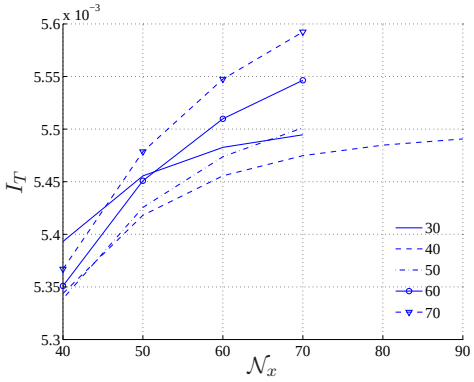

(a) Average of τ_b over T.

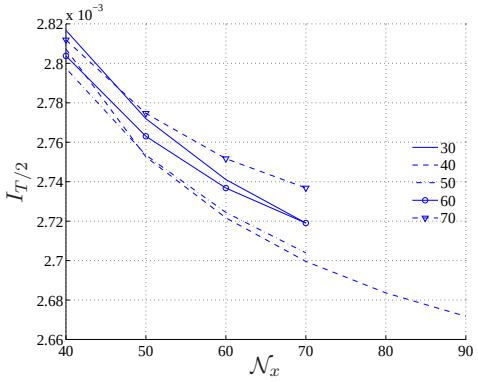

(b) Average of τ_b over $T/2$.

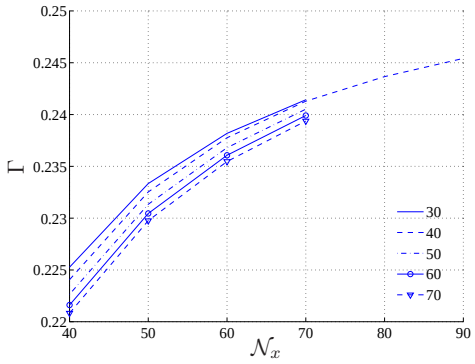

(c) Vortex strength.

Figure 2.8: *Plot of the three quantities I_T, $I_{T/2}$ and Γ for different grid sizes. $\mathcal{N}_x$ being cells in the horizontal and $\mathcal{N}_y$ cells in the vertical direction, see the legend for the variation in the latter. $\mathcal{N}_T$ is 2000 and $y^+ = 0.08$.*

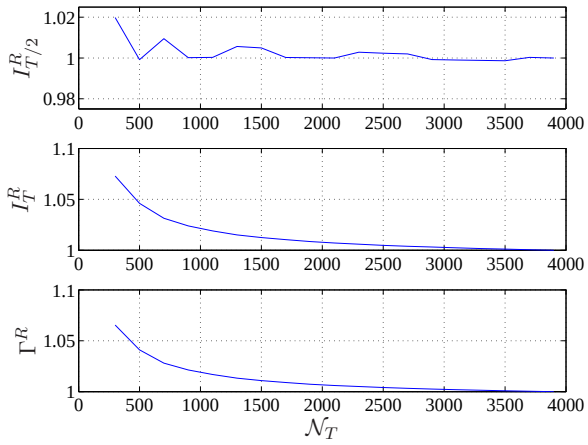

Figure 2.9: *The convergence of the results as a function of* $\mathcal{N}_T$ *for* $\mathcal{N}_x \times \mathcal{N}_y = 50 \times 40$. *The superscript* R *means that the results are relative to those obtained for* $\mathcal{N}_T = 3900$.

is zero. This effect has been investigated and it is concluded that it is of insignificant importance for the rigid bed investigation in chapter 3 but this behaviour can be important when considering the morphological update based on period averaged bed load. A discussion of this and the problems encountered with a clustered point distribution is discussed in section 4.2.

Chapter 3

Flow and Bedload Over Rigid Bed Shapes

The main part of this work considers the flow and sediment transport over rigid bed shapes, where six different shapes have been used. Based on an analysis of these six bed shapes it is the hope that a period average equilibrium shape of ripple under the influence of oscillatory flows can be given.

Further the analysis leads to a detailed analysis of the flow patterns both with respect to the phase resolved flow and with respect to the period averaged flow quantities.

In this chapter the rigid bed shapes and the considered flow is presented. Secondly a phase resolved flow description will be given in terms of the way separation occur on the upstream and lee side of the ripple.

Afterward the period averaged quantities are investigated which will focus on the recirculation cell discussed in section 1.1. The investigated quantities will be the strength of the recirculation zone, the penetration depth and a correlation of these two quantities. Further a correlation of the strength with period averaged bed shear stress is considered.

Having established a good flow description and understanding of the processes, the sediment transport over the different shapes as a function of the Shields parameter, θ, will be given. The sediment transport capacities, $\mathcal{C}_B$, are analysed as a function of the ripple profile.

3.1 Shape of the Rigid Bedforms

The choice of rigid bed shape covers six different shapes and two kinds of crests, namely smooth or sharp. Three of the bedforms are simple analytic functions and the other three are modifications to one of the analytic functions. The analytic functions with a smooth crest are given by a pure

cosine

$$\mathcal{S}_1: \quad h(x) = \frac{h_0}{2}\cos\left(\frac{2\pi}{\lambda}x\right) + \frac{h_0}{2} \tag{3.1}$$

and a cosine added a second harmonic

$$\mathcal{S}_2: \quad h(x) = \frac{h_0}{2}\left\{\cos\left(\frac{2\pi}{\lambda}x\right) + 0.25\cos\left(\frac{4\pi}{\lambda}x\right)\right\} + \frac{3h_0}{8} \tag{3.2}$$

The sharp crested ripple is parabolic and given as

$$\mathcal{S}_{100\%}: \qquad h(x) = \begin{cases} 4h_0\lambda^{-2}\left(x+\frac{\lambda}{2}\right)^2 & \text{for} \quad x < 0 \\ 4h_0\lambda^{-2}\left(x-\frac{\lambda}{2}\right)^2 & \text{for} \quad x \leq 0 \end{cases} \tag{3.3}$$

where λ is the length of the ripple and h_0 the trough-to-crest height. The parabolic shape has been chosen inspired by the analytic finding by Fredsøe and Hedegaard (1983). The length of all of the ripples has been chosen to be $\lambda = 1.2a$ from the consideration in Hedegaard (1985).

The modified bed shapes are based on $\mathcal{S}_{100\%}$ to see the effect of a rounding of the sharp crest. This rounding is created by introducing a part of a circle on top of the parabola, see figure 3.1.

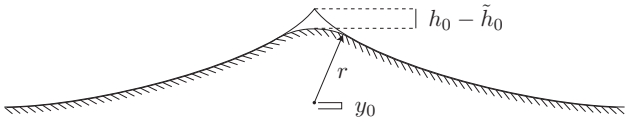

Figure 3.1: *Sketch of the smoothing routine of the parabola to a smooth crested ripple.*

The rounding if defined by the criterion

$$\max\left|\frac{\mathrm{d}\mathcal{S}_f}{\mathrm{d}x}\right| = f\max\left|\frac{\mathrm{d}\mathcal{S}_{100\%}}{\mathrm{d}x}\right| = f\frac{4h_0}{\lambda} \tag{3.4}$$

thus meaning that the maximum slope of the ripple profile should be f times the maximum slope of $\mathcal{S}_{100\%}$. In this way three different bed shapes are introduced, namely $\mathcal{S}_{97\%}$, $\mathcal{S}_{93\%}$ and $\mathcal{S}_{91\%}$. The effective height of the ripple is changed from h_0, since it is not possible to maintain the same height with a reduced slope. All profiles will still be referred to as having the height h_0 as the one given for $\mathcal{S}_{100\%}$ for a matter of comparability.

The height of the crest is written as

$$\tilde{h}_0 = r + y_0 \tag{3.5}$$

where $\tilde{h}_0$ is the reduced height, r is the radius of the smoothing and y_0 is the y-coordinate of the center of the circle. Those are given as

$$r = \frac{(1-f)\lambda^2}{8fh_0}\sqrt{(8fh_0\lambda^{-1})^2 + 1} \tag{3.6}$$

$$y_0 = f^2 h_0 - \frac{(1-f)\lambda^2}{8fh_0} \tag{3.7}$$

The fact that the height is reduced means that the flow is less contracted over the crest. This has to be taken into account when analyzing the results. The reduction in the height is in the order of magnitude $\mathcal{O}(1-f)$ for the present work with $h_0/\lambda \ll 1$. Comparison of the shapes can be seen for $\mathcal{S}_1$, $\mathcal{S}_2$, $\mathcal{S}_{91\%}$ and $\mathcal{S}_{100\%}$ in figure 3.2. The shapes of $\mathcal{S}_{93\%}$ and $\mathcal{S}_{97\%}$ will be in between $\mathcal{S}_{100\%}$ and $\mathcal{S}_{91\%}$.

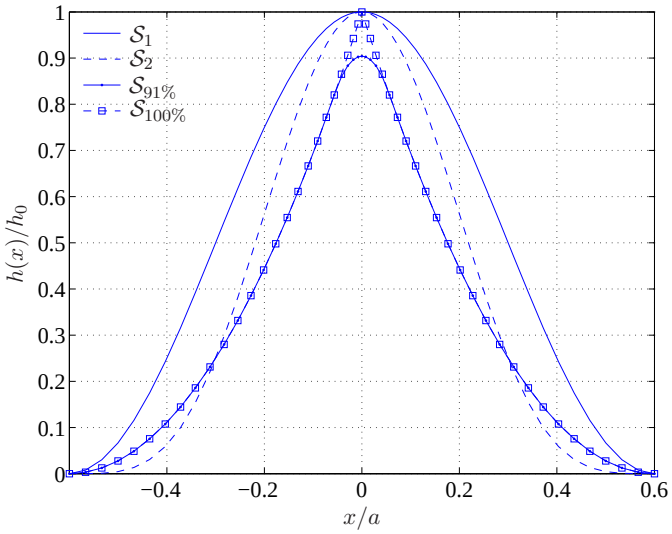

Figure 3.2: *Four of the bed shapes with heights relative to* h_0.

The steepness of the bed shapes varies in the range $h_0/\lambda \in [0.00,\ 0.158]$, which is the limiting steepness for $\mathcal{S}_2$, i.e. the maximum slope exceeds the angle of repose of the sand. The test cases are summarized in table 3.1. In this θ_0 is the maximum Shields parameter on a flat bed.

The theoretical and the modeled ratio of the Shields parameter to the critical one deviates significantly. This is explained by figure 2.5 in Fredsøe and Deigaard (1995), where the data points for $a/k_N = 130$ deviates from the expression in (2.22). In the following θ_0/θ_c calculated by Dune2D will be referred to as $\mathcal{M}$.

As can be seen in table 3.1 $w_s/U_m > 0.20$ for all the test cases, thus it is reasonable to exclude suspended sediment transport (see Andersen, 1999).

Table 3.1: *A summary of the parameters used in the present investigation of flow over rigid bed forms.*

	$Re_a \cdot 10^{-5}$	a/k_N	θ_0/θ_c, (2.22)	θ_0/θ_c, Dune2D	Deviation	w_s/U_m
A :	1.527	130.0	1.00	1.31	31%	0.310
B :	3.903	130.0	1.60	2.15	34%	0.256
C :	6.144	130.0	2.00	2.74	37%	0.231
D :	9.601	130.0	2.50	3.45	38%	0.208

Further $\mathcal{N}_T = 1000$, $\mathcal{N}_S = 10$, $\Delta Q_0 = 10^{-6}$ and $y^+ = \mathcal{O}(0.08)$ has been used.

3.2 Phase-Resolved Flow Description

In this section the phase resolved flow properties will be considered. These are vortex generation through flow separation and the direction of the horizontal component of the near bed velocity. This is used to specify the phase lag between flow separation and the free stream velocity; this is done for both the upstream and lee side of the ripple, termed ϕ_+ and ϕ_- respectively. Based on these results three kinds of vortex generation is presented.

First a qualitatively description of the flow quantities and the general physical mechanisms behind the different observations will be given in section 3.2.1. To keep the length of this analysis reasonably, results for $\mathcal{S}_{97\%}$ are the only to be presented.

Then a quantitatively description of the phase lag will be given in section 3.2.2, where the phase lag will be connected to the different kinds of flow separation.

Finally a preliminary discussion of the influence of the different types of flow separation on the bed load transport will be presented. The detailed analysis of the bed load transport is presented in section 3.4.

3.2.1 Qualitatively Description of Flow Separation on the Lee Side

In figure 3.3, the vorticity for three different steepnesses are plotted for the phase $\omega t = 90°$. The red color is identical to positive vorticity, i.e. clockwise rotation, and the blue color is negative vorticity. Vorticity larger than 40 have been removed from the data set to make the important features visible. The vorticity is used, since the initiation of separation is hard to seen in a simple vector plot of the velocity field.

For the smallest steepness, see figure 3.3(a), the vorticity is positive along the entire bed, thus no separation has occurred at the present state on the lee side of the ripple. For the steepness in between, see figure 3.3(b), it is seen that the positive part of the vorticity has values less than the threshold close to the bed. Actually a small area of negative vorticity is present at the crest, but this is not visible in the figure. This illustrates the initialization of flow separation at the bed. For the steepest ripple, see figure 3.3(c), there is a thin layer of negative vorticity on the lee side of the ripple and the separation is in a mature state.

Due to the nature of waves, flow separation must occur each half period, but figure 3.3 shows that the separation takes place for different phases as a function of the ripple steepness. The actual point of separation has been investigated for the three cases. The horizontal component of the near bed velocity, $U_b(x,t)$, is plotted in figure 3.4 for the x-coordinate, where separation is initialized. The initialization is defined as the first occurrence of a negative velocity on the lee side of the ripple, see figure 3.6 for a definition

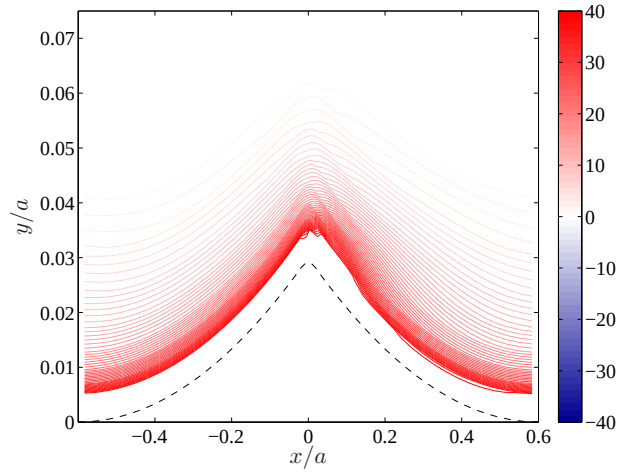

(a) $h_0/\lambda = 0.025$

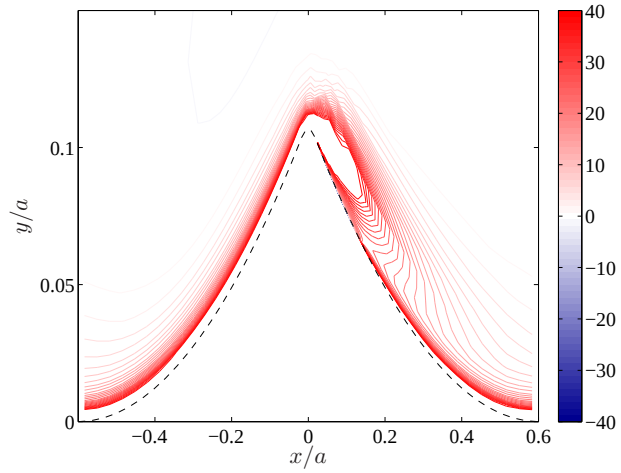

(b) $h_0/\lambda = 0.092$

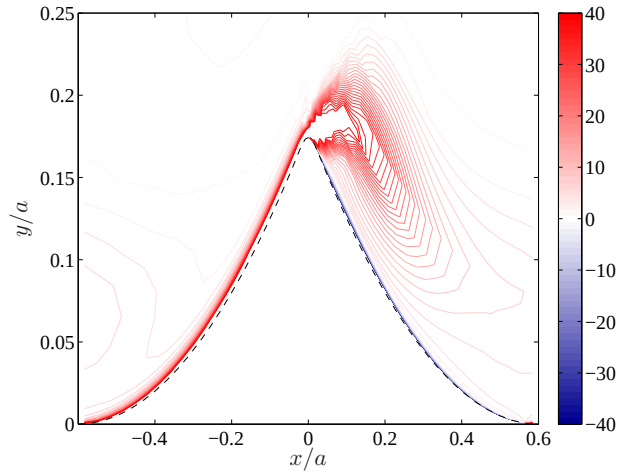

(c) $h_0/\lambda = 0.150$

Figure 3.3: *The vorticity over* $\mathcal{S}_{97\%}$ *at* $\omega t = 90°$ *for varying steepness. All are plotted for test case* **D**. *The dashed line is the ripple.*

sketch. The phase, where separation occurs, is marked by a red square in figure 3.4. The phase resolved plot supports the results in figure 3.3, because for the small steepness, flow separation does not occur before $\omega t = 153°$, the intermediate steepness has flow separation at $\omega t = 80°$ and for the steepest ripple the separation is completely out of phase with the free stream velocity, i.e. separation occurs at $\omega t = 0°$.

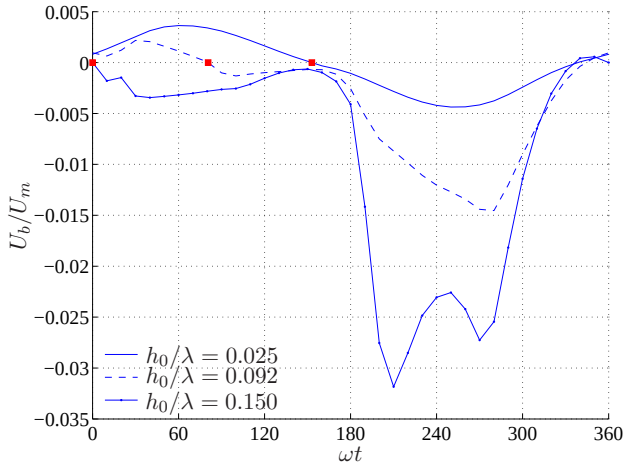

Figure 3.4: *The near bed horizontal velocity, U_b, in the point where separation is initialized on the lee side of the ripple. The ripple profile is $\mathcal{S}_{97\%}$ and the red squares are the phases where separation occurs.*

The separation for $h_0/\lambda = 0.025$ occur at such a late state that it correspond to the phase lag on a flat bed, which is determined to be $27° - 30°$ for $a/k_N = \mathcal{O}(100)$ (see Dixen *et al.*, 2007). Due to the small steepness, this ripple is in the rolling grain ripple regime, thus this result is expected due to the lack of vortex generation.

The movement of the vortex for $h_0/\lambda = 0.150$ is similar to the mechanism reported by Fredsøe *et al.* (1999), where a volume of fluid with opposite rotation is washed over the crest together with the main vortex. This volume remains attached to the ripple crest and initiate the growth of the following vortex.

The third kind of separation has not been seen reported. This is probably because other authors used a combination of rather steep and sharp crested ripples, and as will be seen in section 3.2.2 this kind of separation occur exclusively for intermediate ripple heights and relatively smooth crests. In this case, separation occur around $\omega t = 90°$, i.e. when the free stream reaches its maximum outer velocity and the global pressure gradient is approximately 0. Due to the contraction of the flow at the crest there will be a lower pressure on the crest than the in trough. This results in an

adverse pressure gradient which apparently is strong enough to cause flow separation.

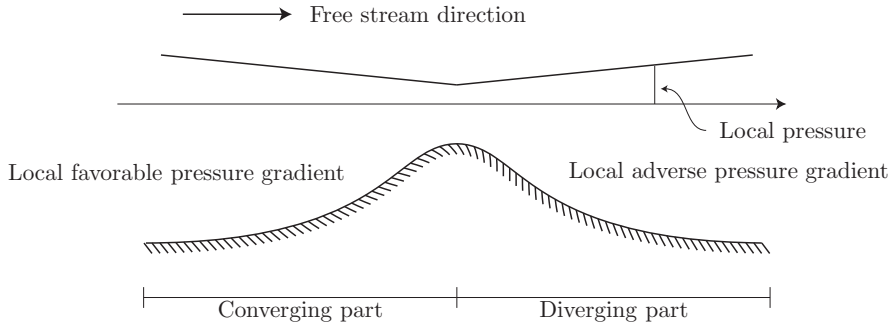

Figure 3.5: *Definition sketch of the pressure over the ripple, and thus the working pressure gradients.*

This further gives the anticipation to the following analysis that the flow separation on the lee side of the ripple will occur with an increasing phase lag to the outer flow when the ripple increases in steepness, because the pressure gradient due to expansion of the cross section gives an additional adverse pressure gradient on top of the global one, see figure 3.5. Thus an earlier separation is expected. Similarly a later separation due to flow reversal on the upstream side is expected, as the adverse pressure gradient on the lee side acts in the opposite direction, i.e. as a favorable pressure gradient on the upstream side due to the periodicity of the model.

3.2.2 Quantitatively Description of the Flow Separation

One of the most significant features in the phase resolved flow is the flow separation, which in the above is seen to vary with the steepness of the ripple. In the following a quantitative analysis is given on this mechanism for all bed shapes and all steepnesses. Both the upstream and lee side separation are considered. The upstream separation relative to the free stream velocity, ϕ_+, is defined as the phase where U_b, measured just upstream of the crest, changes sign from positive to negative in the interval $\omega t \in [0°, 180°]$. This definition is chosen since the separation zone expands from the downstream side to the upstream side, thus considering the entire upstream side would yield erroneous results, see figure 3.6 for a definition sketch.

Regarding the lee side separation it is defined as the phase where the sign of U_b first becomes negative. The phase is not as rigidly restricted to a phase interval since the flow separation on the lee side can lead over the free stream velocity with more than 180°.

An analysis of the two separation points are carried out for all shapes and all test case. The results are to be seen in the figures 3.7(a)-3.7(f). The

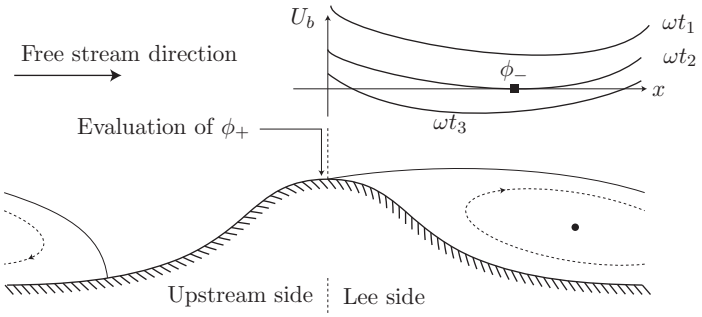

Figure 3.6: *Sketch of the definition of the separation on the upstream and lee side of the ripple. The upstream side is defined at the crest due to the expansion of the vortex over the trough. Separation on the lee side is defined where it first occurs; here* $\omega t_1 < \omega t_2 < \omega t_3$.

results will be discussed in details in the following.

1. The phase lag on a flat bed corresponds to the phase lag found experimentally. Several experimental investigations are compiled by Dixen *et al.* (2007).

2. The upstream phase lag, ϕ_+, follows the expected trend for all shapes up to a certain steepness. In this interval the phase lag decreases and it can only be explained by the increase in inertia of U_b due to convective acceleration on the converging part of the ripple. This acceleration must the driven by a favorable pressure gradient which counter acts the global adverse pressure gradient, thus a decrease in the phase lag is the result. The increase in ϕ_+ on steeper profiles has not been explained, but is noted to be correlated with the large phase lags in ϕ_-.

3. For the downstream phase lag, ϕ_-, three different kinds of separation, described in 3.2.1, are found. For the very gentle profiles, namely $\mathcal{S}_1$ and $\mathcal{S}_2$, there is an extremely gentle transition from the flat bed phase lag to a larger one. This increase in phase lag is due to the additional adverse pressure gradient on the lee side of the ripple and the smaller U_b on the lee side.

   For the parabolic shaped ripples there is a more pronounced and almost discontinuous jump between the three types of separation. It is seen that the less the parabolic shaped ripple is smoothed, the smaller the steepness is needed for the separation to come out of phase with the free stream velocity. Actually the intermediate flow separation zone tends to be decreased significantly and the flow goes more or less from flow reversal separation to out of phase reversal. This faster transition

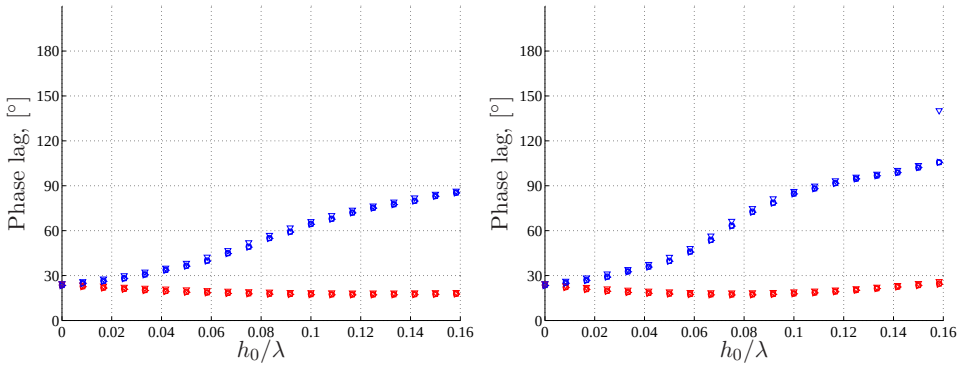

(a) Ripple shape $\mathcal{S}_1$

(b) Ripple shape $\mathcal{S}_2$

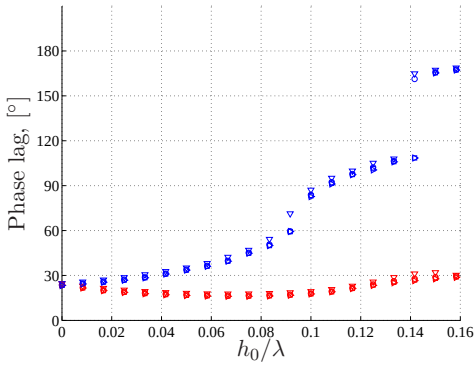

(c) Ripple shape $\mathcal{S}_{91\%}$

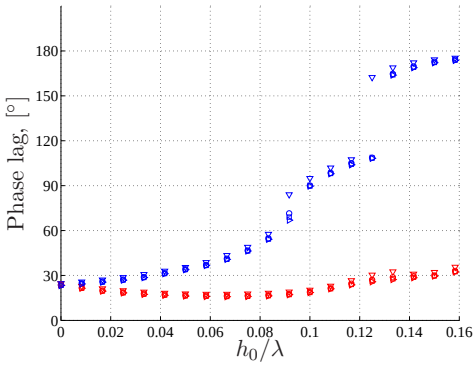

(d) Ripple shape $\mathcal{S}_{93\%}$

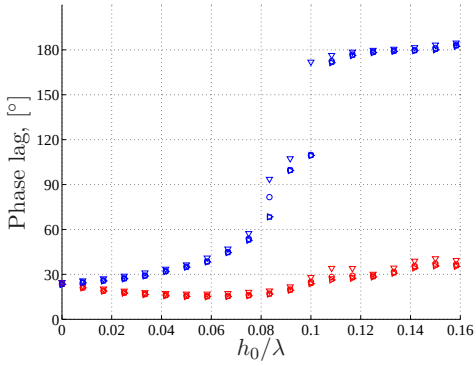

(e) Ripple shape $\mathcal{S}_{97\%}$

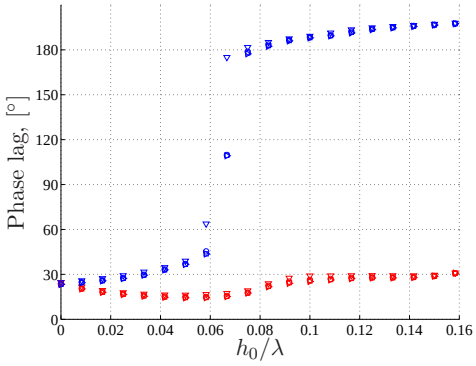

(f) Ripple shape $\mathcal{S}_{100\%}$

Figure 3.7: *The upstream and lee side phase lag between the point of separation and the free stream velocity. The data is plotted for all shapes.*
Red: ϕ_+. *Blue:* ϕ_-. $\triangledown$*: Test case* **A**. $\circ$*: Test case* **B**. $\square$*: Test case* **C**. $\triangleleft$*: Test case* **D**.

to out of phase vortex generation must be due to the volume of fluid carried over the crest at the point of flow reversal, which more easily gets hold on the crest, so it can initialize the vortex generation.

4. It is seen from the data sets that there is approximately no dependence on the Reynolds number, thus only one data set will be plotted in the following flow analyses.

In figure 3.8 the location of the separation point is plotted against the lee side phase lag. From this, two thing are seen, namely that as the phase lag increases from the flat bed value, the point of separation moves toward the crest. Further it is seen that the point of separation is located almost at the crest for the out of phase separation, which fits well with the mechanism of having one vortex washed over from the opposite side of the ripple and being attached to the crest and hereby initiate the separation.

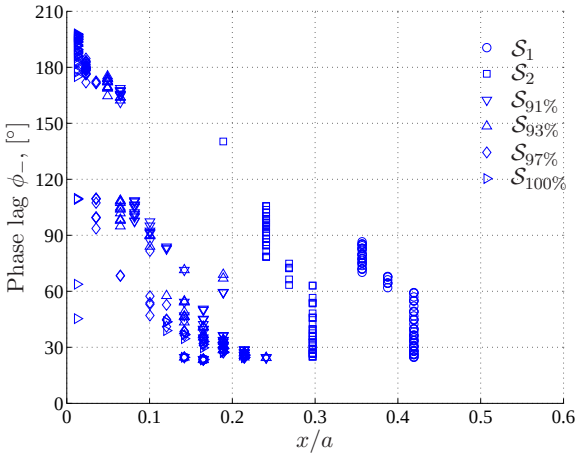

Figure 3.8: *The phase lag on the lee side of the ripple, ϕ_-, as a function of the distance from the crest where separation occur.*

3.2.3 Comments on the Vortices

First it is to be noted that based on an analysis of the numerical results, it looks like the rule of thump that vortex ripples appears when h_0/λ exceeds 0.10 is qualitatively well. There is some shape dependence, especially for $\mathcal{S}_{97\%}$ and $\mathcal{S}_{91\%}$, where the vortex is present for smaller steepnesses.

Secondly, assuming that the steepness is large enough, the vortices tends to appear in two different ways. These ways are governed by the sharpness of the crest, and the groups consist of $\mathcal{S}_1$, $\mathcal{S}_2$ and $\mathcal{S}_{91\%}$ in the first and $\mathcal{S}_{93\%}$, $\mathcal{S}_{97\%}$ and $\mathcal{S}_{100\%}$ in the second. The difference in appearance is sketched in figure 3.9.

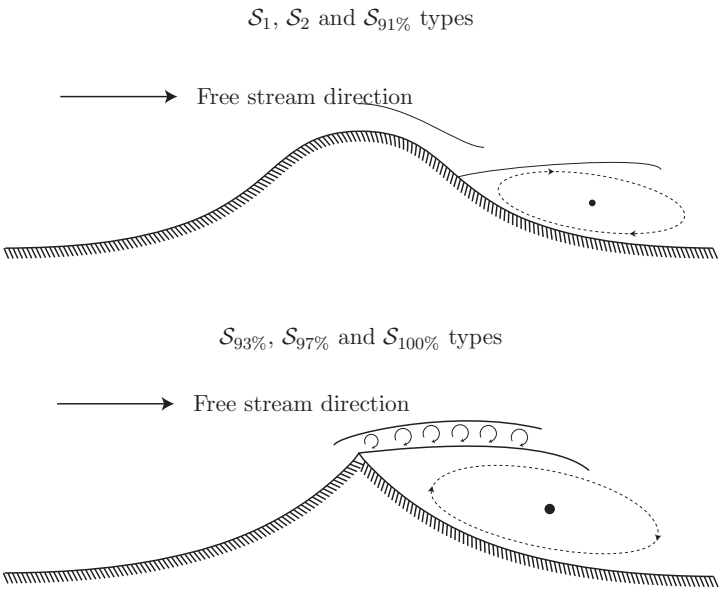

Figure 3.9: *Two types of vortices generated on the lee side of the vortex, the first separates some distance from the crest on the lee side, and the second separates qualitatively at the crest.*

The two different groups is governed by the sharpness of the crest, and for the smooth type of ripple profiles, the top panel in figure 3.9, the flow remains attached at the lee side of the ripple until some distance from the crest, where the adverse pressure gradient become to large. This attached flow remains attached until the flow separation due to flow reversal, thus the vortex does not grow in the direction of the crest. The second type of vortex, the lower panel in figure 3.9, is separated at the crest, at least qualitatively. The rounded parabolic shapes does tend to have a short distance on the lee side where the near bed velocities are directed in the freestream direction, but this distance is qualitatively neglectable.

3.2.4 Preliminary Discussion on Bed Load Transport

Due to the large deviation in the phase where separation occur on the lee side, a direct effect on the sediment transport must be expected. Figure 3.4 illustrates this influence well. This figure shows the occurrence of separation along the ripple for different steepnesses.

For the smallest steepness, the near bed velocity is almost sinusoidal distributed centered around a zero mean. The effect of earlier separation is that the period averaged near bed velocity becomes more and more negative, thus the period averaged sediment transport will probably have a crest directed component until the gravity effect becomes large enough. For the

steepest ripple there is almost no positive component, and from the previous analysis, this point is seen to be situated at the crest, thus this indicates that the extremely sharp, i.e. large curvature of the crest, cannot be stable in terms of a period averaged profile.

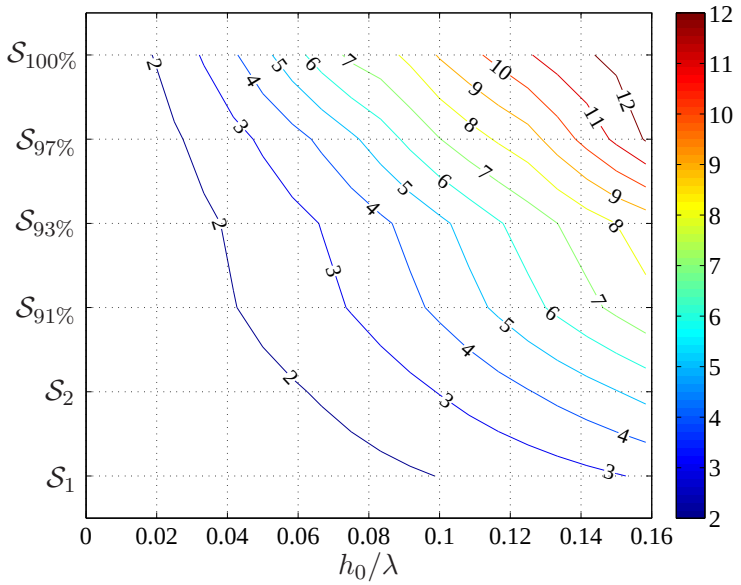

Figure 3.10: *The amplification factor of the maximum bed shear stress due to an increase in the steepness. The amplification factor is given for all shapes.*

Another feature, which has direct influence on the bed load transport is the Shields parameter. In figure 3.10 the amplification of the maximum bed shear stress due to the increase in steepness is depicted. This shows that for $\mathcal{S}_{100\%}$ the amplification in the maximum bed shear stress, and therefor directly an amplification of the maximum Shields parameter, exceeds 12 for the steepest of this bed shape. This means that even for test case **A** the maximum Shields parameter will be close to the limit of sheet flow, commonly accepted at $\theta = 0.8$. This support the analysis based on the phase lag, ϕ_- that the sharp ripple profile is highly unlikely to be the period averaged equilibrium shape, as the transport will be large and therefor the profile will be eroded at the crest.

The more round crested ripples on the other hand, namely at least up to $\mathcal{S}_{91\%}$, have smaller amplification factors thus there is a less drastic increase in the Shields parameter. Thus this amplification factor further supports the discussion that with a less pronounced separation at the lee side of the ripple gives longer time for down slope sediment transport, which can help stabilizing the profile. The transport capacity along the ripple side and the

stability of the ripples is discussed in section 3.4. Further the influence on the amplification factor by a dynamically moving crest is discussed in section 4.1.

The increase in amplification factor as the sharpness of the ripple crest is increased has to be shape related. This is stated as the steepness is the same for $\mathcal{S}_1$ and $\mathcal{S}_{100\%}$, but there is a factor of 4 in difference. This factor must originate from the convective acceleration of the water along the ripple profile. In the case of $\mathcal{S}_1$ this acceleration takes place gradually, thus the thickness of the boundary layer has time to be developed along the ripple profile. In the case of $\mathcal{S}_{100\%}$ the opposite happens, as the slope of the ripple steadily increases, and thus the local acceleration happens over such a short distance that the development in the boundary layer thickness will be insignificant compared to the contraction of the flow and thus increase the near bed velocity.

3.3 Description of the Period Averaged Flow

In this section the period averaged flow description will be given. The period averaged flow quantity is as already discussed the recirculation zone spanning over half a ripple length from trough to crest. The height of the recirculation zone is defined as the penetration depth, δ_P.

First a qualitatively description of the recirculation zone as a function of the bed shape and the steepness will be considered. Afterward a more quantitative description will be given based on calculated penetration depths, recirculation strengths and shape dependence.

3.3.1 Qualitatively Description of the Recirculation Zone

Two different kinds of period averaged flow over ripples are given in the following. In figure 3.11 the period averaged flow for a small steepness is given for all six shapes. In figure 3.12 the same is plotted just for a larger steepness. As the period averaged flow quantities are found to be Reynolds independent the results are only plotted for test case **D**.

These figures show first of all that there are recirculation cells in the period averaged quantities in oscillatory flows over ripples as long as the height is different from 0.

When comparing the flow for the six shapes for $h_0/\lambda = 0.05$ there is hardly any difference to be seen. The height of the recirculation zone is approximately constant and the velocities are in the same order of magnitude. The differences in the current magnitude must be attributed to the differences in the curvature of the bed shape and thus different locations where the convective acceleration takes place.

For $h_0/\lambda = 0.15$ a significantly different pattern is seen, because in this case the flow is highly bed shape dependent. The following shape specific features can be identified just from looking at the figures 3.12(a)-3.12(f):

1. The steeper the ripple the larger the near bed velocities. The importance of the steepness is clearly illustrated by comparing $\mathcal{S}_2$ and $\mathcal{S}_{93\%}$. Despite the actual height of $\mathcal{S}_2$ being larger than $\mathcal{S}_{93\%}$, see section 3.1, the current velocities for $\mathcal{S}_{93\%}$ are in the order of magnitude 15% larger in the case of the smoothed parabola.

2. The steeper the ripple becomes, the more pronounced are the vertical velocity components at the crest. This influences greatly the height of the recirculation zone, since a larger vertical velocity will reach deeper into to the main flow measured from the bed shape. In section 3.3.2 it will be shown that the vertical velocity distribution along the vertical over the crest plays a significant rôle in the strength of the recirculation zone.

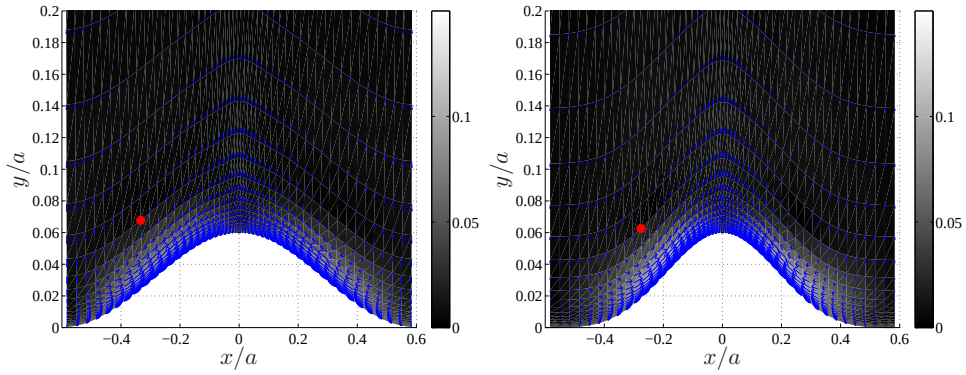

(a) $\mathcal{S}_1$, $h_0/\lambda = 0.05$ (b) $\mathcal{S}_2$, $h_0/\lambda = 0.05$

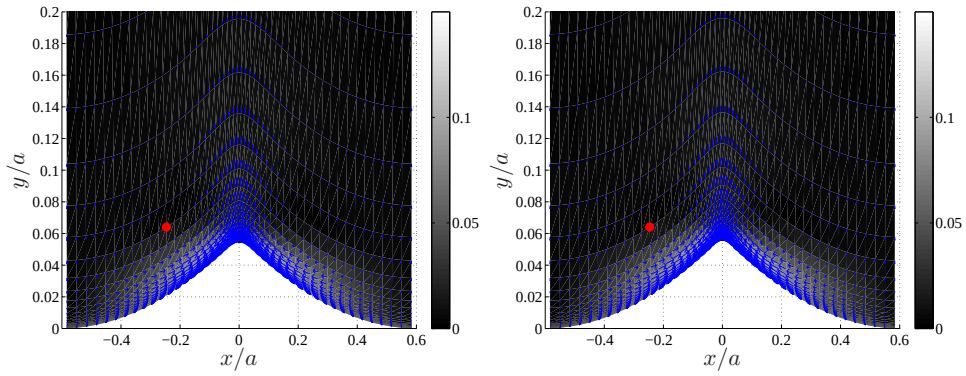

(c) $\mathcal{S}_{91\%}$, $h_0/\lambda = 0.05$ (d) $\mathcal{S}_{93\%}$, $h_0/\lambda = 0.05$

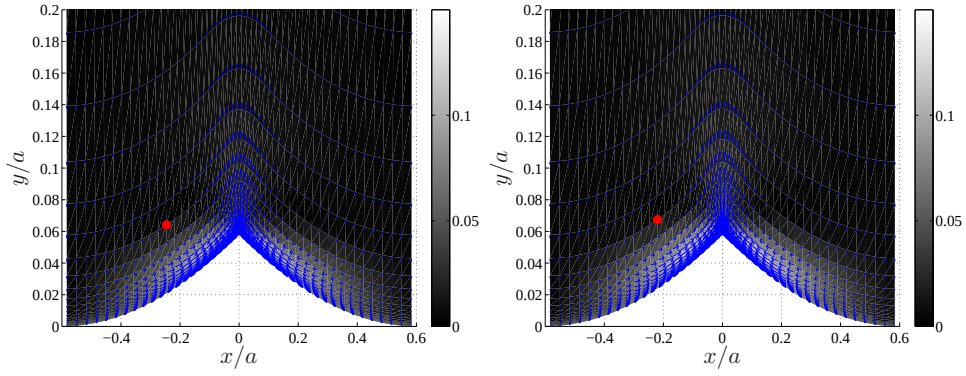

(e) $\mathcal{S}_{97\%}$, $h_0/\lambda = 0.05$ (f) $\mathcal{S}_{100\%}$, $h_0/\lambda = 0.05$

Figure 3.11: *The recirculation zone over the six different bed forms for a steepness of* $h_0/\lambda = 0.05$. *Results from test case* **D**. *The surface plot gives the magnitude of the velocity vector, namely* $\overline{W}/U_m = \sqrt{\overline{U}^2 + \overline{V}^2}/U_m$. *The red dot is the approximate center of the recirculation cell.*

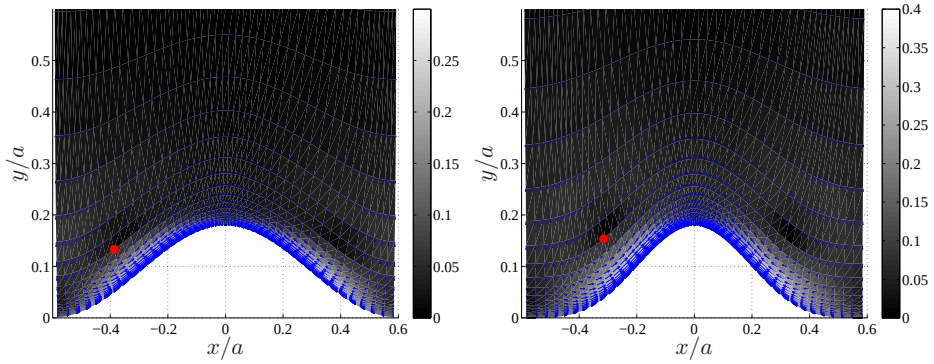

(a) $\mathcal{S}_1$, $h_0/\lambda = 0.15$

(b) $\mathcal{S}_2$, $h_0/\lambda = 0.15$

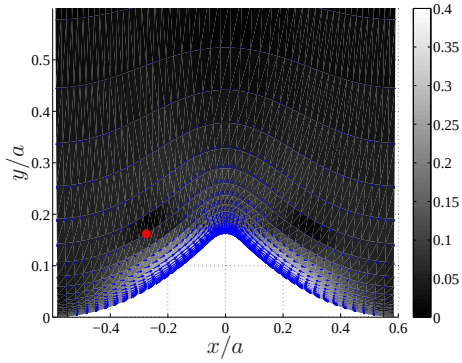

(c) $\mathcal{S}_{91\%}$, $h_0/\lambda = 0.15$

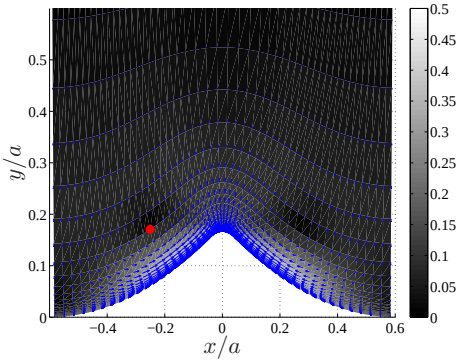

(d) $\mathcal{S}_{93\%}$, $h_0/\lambda = 0.15$

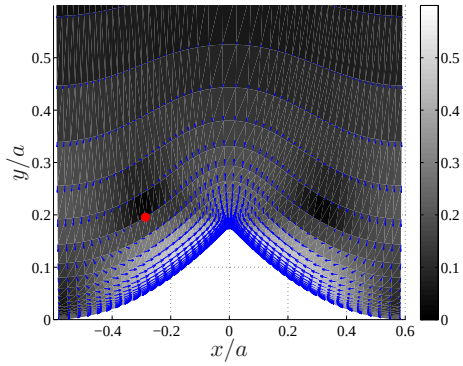

(e) $\mathcal{S}_{97\%}$, $h_0/\lambda = 0.15$

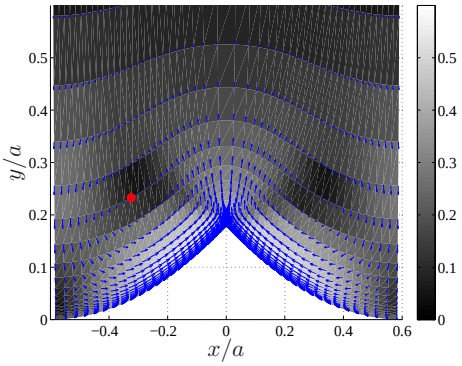

(f) $\mathcal{S}_{100\%}$, $h_0/\lambda = 0.15$

Figure 3.12: *The recirculation zone over the six different bed forms for a steepness of* $h_0/\lambda = 0.15$. *Results from test case* **D**. *The surface plot gives the magnitude of the velocity vector, namely* $\overline{W}/U_m = \sqrt{\overline{U}^2 + \overline{V}^2}/U_m$. *The red dot is the approximate center of the recirculation cell. Be aware of the different scales.*

3. The approximate center of rotation of the recirculation zone is greatly effected by the bed shape. In the figures 3.12(a)-3.12(d) the trend is that the center moves away from the bed and toward the crest. For the last two bed shapes, see figure 3.12(e)-3.12(f) the opposite happens, namely that the center of rotation moves away from the crest.

The significant change in the flow from $h_0/\lambda = 0.05$ to $h_0/\lambda = 0.15$ reveals that the period averaged properties of the flow changes significantly when moving from the rolling grain ripple regime to the vortex ripple regime.

3.3.2 Quantitatively Description of the Recirculation Zone

In figure 3.13 the strength of the recirculation cell over the computational domain A, see section 3.1, is plotted. The rotational strength is calculated as

$$A\Gamma = \int_A \overline{\Omega} \mathrm{d}A \tag{3.8}$$

From the figure it is seen that the strength grows with the steepness of the ripple which is expected as the more convergent/divergent the flow becomes, the larger the difference between the bed shear stress in the half period with convergent and the half period with divergent flow.

This effect is quite insignificant compared to the significance of the actual shape of the ripple, where it is seen that $\mathcal{S}_1$ results in the smallest strength and $\mathcal{S}_{100\%}$ in the largest one. Further $A\Gamma(\mathcal{S}_2) \simeq A\Gamma(\mathcal{S}_{91\%})$.

The strength of the recirculation zone can be put up against the phase at which separation occur. From this comparison it is seen that in general, the stronger the vortex the more out of phase the flow separation is with the free stream flow. The difference in phase lag does not govern it completely as $\phi_-(\mathcal{S}_{91\%}) > \phi_-(\mathcal{S}_2)$ but the recirculation strength is almost identical. Thus the shape and steepness of the ripple must be influencing as well. The comparison of strength and phase lag is discussed more detailed later in this section.

It should be noted that these strengths are calculated over the entire height of the domain, thus figure 3.13 gives the averaged rotational strength over the computational domain and not the actual strength, which only works over a part of the domain.

Therefore the penetration depth, see definition in figure 3.14, has been estimated. The procedure of determining δ_P is first to evaluate the following integral

$$I_U(y) = \int_{\lambda/(2a)}^{\epsilon(y)} \overline{U}(x, y) \mathrm{d}x \tag{3.9}$$

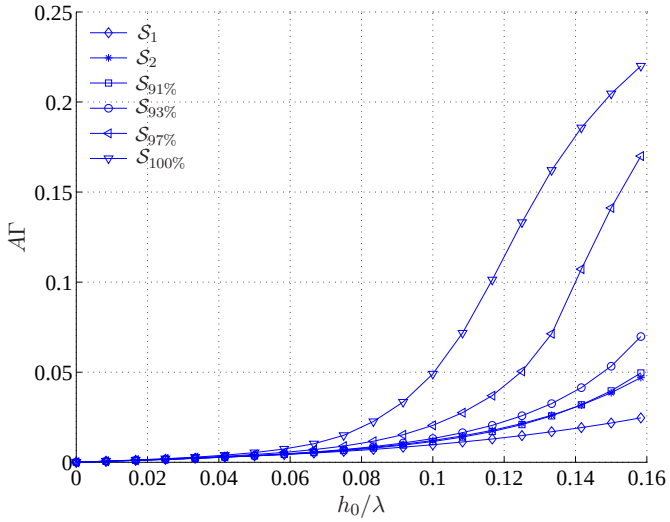

Figure 3.13: *The strength of the recirculation cell over the computational area A. The results are plotted for test case* **D**.

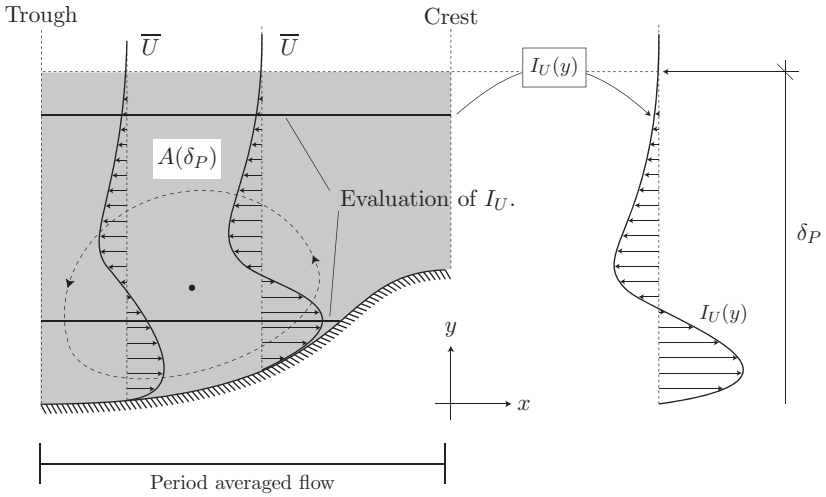

Figure 3.14: *Sketch of the evaluation of $I_U(y)$ together with the formal definition of the penetration depth δ_P.*

where

$$\epsilon(y) = \begin{cases} h^{-1}(y)/a & \text{for} \quad y/a < h_0/a \\ 0 & \text{for} \quad y/a \geq h_0/a \end{cases} \tag{3.10}$$

Due to symmetry and D/a being so large that the flow is uninfluenced by the upper boundary

$$\int_0^{D/a} I_U(y)\mathrm{d}y = 0 \tag{3.11}$$

From (3.9) δ_P has been defined as

$$\frac{|I_U(\delta_P)|}{\max|I_U(y)|} = 0.01 \tag{3.12}$$

i.e. the distance from the bed, where I_U becomes 1% of the maximum of $I_U(y)$.

To illustrate the results from this analysis $I_U(y)$ for all shapes and for $h_0/\lambda = 0.05$ and $h_0/\lambda = 0.15$ is plotted in figure 3.15(a)-3.15(b). From these it is seen that for small steepnesses the results are remarkably the same. The penetration depth, δ_P, is the same for all shapes and the differences in the maximum can be explained by differences in the curvature of the ripple profile. For larger steepnesses huge differences occur. The penetration depth is only changed a little and is in the same order of magnitude for all shapes. On the other hand the maximum value of I_U deviates significantly from shape to shape. This must be explained by the larger rotational strength for the steepest of the ripples which again is a consequence of earlier flow separation.

Taking δ_P as the actual height of the recirculation zone, the strength of the recirculation zone is modified as

$$A(\delta_P)\Gamma_0 = A\Gamma \tag{3.13}$$

where Γ_0 is the strength of the recirculation zone and $A(\delta_P)$ is the hatched area in figure 3.14. Γ_0 is plotted in figure 3.16(a). As can be seen from these, there is more or less just a factor difference in the results between figure 3.13 and 3.16(a). This observation leads to plotting δ_P as a function of h_0/λ and a nice correlation has been found, see figure 3.16(b). These results does not have direct influence on the current analysis, since the two-dimensionality of the flow is not important for the bed load transport, though it is highly important when considering suspended sediment transport. The effect on the suspended sediment is due to having light sediment and large penetration depth, then the suspended sediment cannot come out of suspension thus the suspended sediment is of little significance on the redistribution of sediment. The opposite argumentation can be taken with small penetration and relatively large fall velocity.

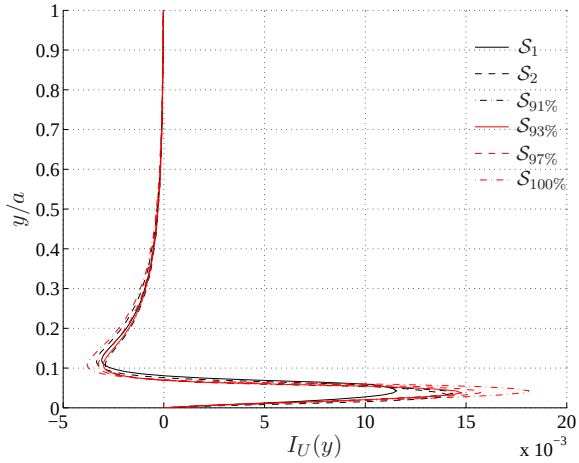

(a) $h_0/\lambda = 0.05$

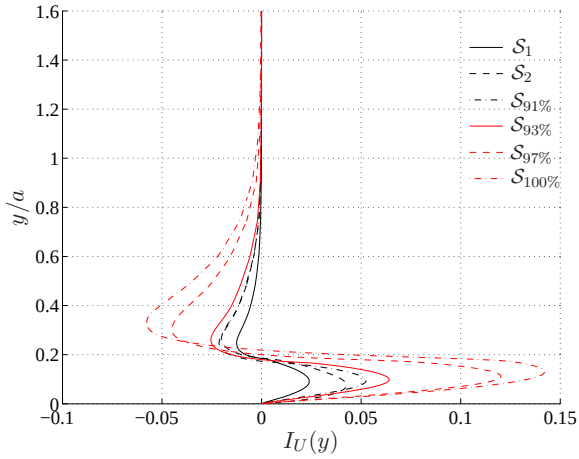

(b) $h_0/\lambda = 0.15$

Figure 3.15: $I_U(y)$ *for all shapes for two different heights. The results are plotted for test case* **D**.

Until now it is only the different mechanisms occurring in the flow, which have been analysed as a function of the bed shape and height. The actual mechanism behind driving the recirculation has not been given any attention. This is done in figure 3.17, where the strength of the recirculation zone

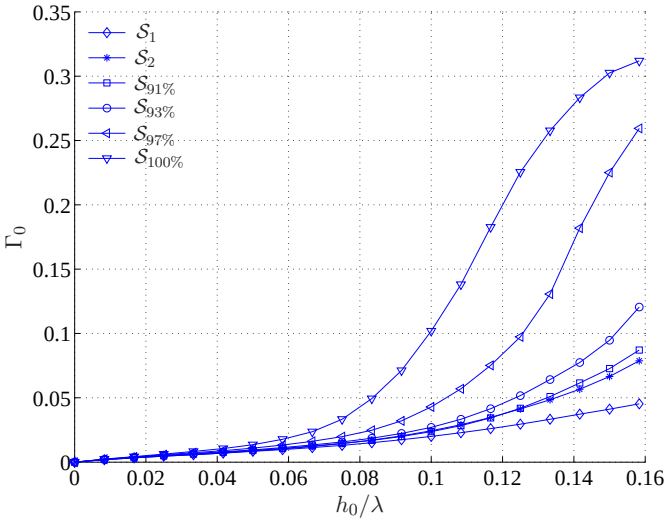

(a) Γ_0, δ_P-corrected, test case **A**.

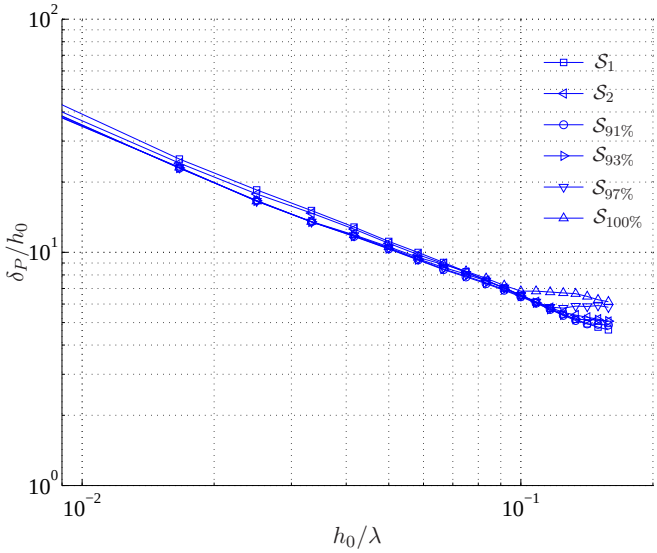

(b) δ_P, test case **A**. .

Figure 3.16: *The area corrected recirculation strength,* Γ_0 *and the relation between the penetration depth as a function of ripple steepness.*

is plotted against the average bed shear stress, namely

$$I_\tau = \frac{1}{\int_0^{1/2} \|\mathbf{h}'(S)\| \mathrm{d}S} \int_0^{1/2} \overline{\tau}_b \|\mathbf{h}'(S)\| \mathrm{d}S \tag{3.14}$$

As this is the driving force, the clear correlation between the strength of the recirculation and the acting force is not surprising.

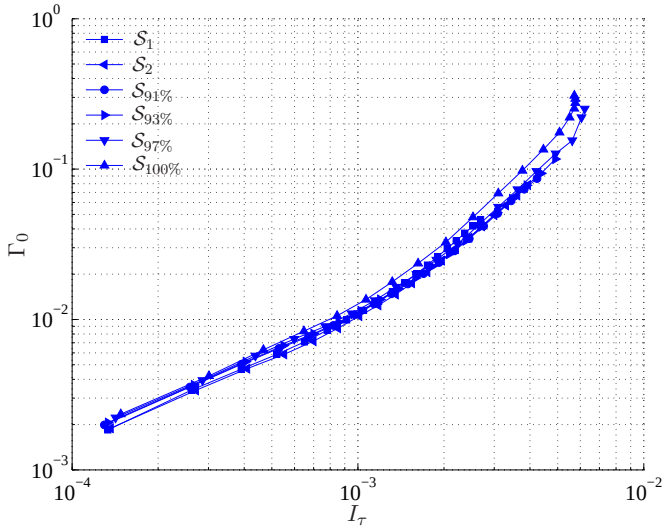

Figure 3.17: *The strength of the recirculation,* Γ_0*, as a function of the driving force,* I_τ*. The data has been plotted for all bed shapes and test case* **B**.

The increase in period averaged bed shear stress is due to the combined convergence and divergence of the flow as discussed in section 1.1. It is interesting how this quantity correlates with the phase lag in the flow separation, since earlier separation is expected to increase the strength of the vortex generated every half period. This comparison can be seen in figure 3.18.

No universal trend is to be seen due to significant shape dependence. The results from the parabolic shaped ripples falls on top of each other until a certain point where the actual shape of the crest can be felt. As expected this happens the earliest for $\mathcal{S}_{100\%}$ and the latest for $\mathcal{S}_{91\%}$. Even though it is highly shape dependent there is a trend toward larger phase lag with increasing I_τ and thus increasing strength of the recirculation zone. Though it should be emphasized that the phase lag, and thus the growth time for the vortex, does not account for everything.

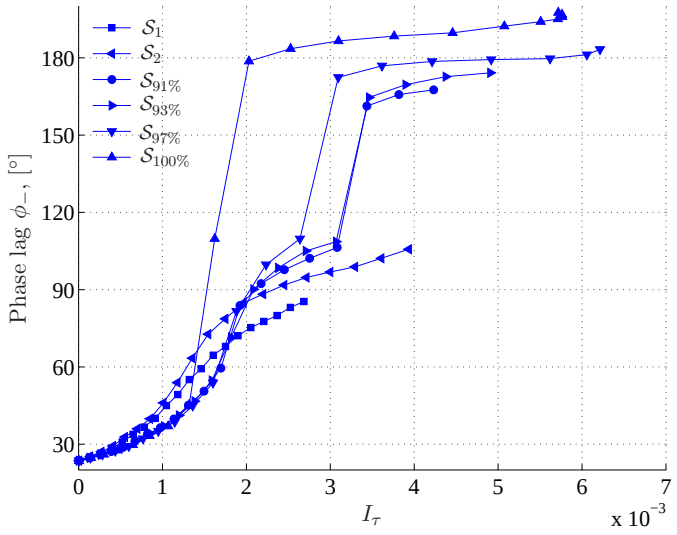

Figure 3.18: *The phase lag on the lee side of the ripple, ϕ_-, as a function of the period averaged bed shear stress I_τ.*

Re-Evaluation of Γ

The introduction of $I_U(y)$ leads to another interesting feature. This is achieved by considering the definition of I_Ω, which rewritten gives

$$\begin{aligned}\Gamma A &= \int_A \overline{\Omega}\mathrm{d}A = \int_0^{D/a}\int_{-\lambda/(2a)}^{\epsilon(y)} \left[\frac{\partial \overline{U}}{\partial y} - \frac{\partial \overline{V}}{\partial x}\right]\mathrm{d}x\,\mathrm{d}y \\ &= \int_0^{D/a}\left[\frac{\partial}{\partial y}\int_{-\lambda/(2a)}^{\epsilon(y)} \overline{U}\mathrm{d}x - \overline{U}(\epsilon(y),y)\frac{\partial \epsilon(y)}{\partial y}\right]\mathrm{d}y - \int_0^{D/a} \overline{V}\Big|_{-\lambda/(2a)}^{\epsilon(y)}\mathrm{d}y\end{aligned}$$

Using the no-slip condition for $\overline{U}$ and $\overline{V}$ and $I_U(0) = 0$ this is reduced to

$$\Gamma A(\delta_P) = I_U(\delta_P) - \int_{h_0/a}^{\delta_P} \overline{V}(0,y)\mathrm{d}y + \int_0^{\delta_P} \overline{V}\left(\frac{\lambda}{2a}, y\right)\mathrm{d}y \qquad (3.15)$$

where a general upper bound is inserted, namely the penetration depth δ_P. This shows that if δ_P is chosen such that $I_U(\delta_P) = 0$, i.e. outside the sphere of influence by the near bed flow, the strength of the rotation is completely determined by the vertical velocity distribution over the trough and the crest. The mechanism in driving the recirculation zone can then be considered as the vertical velocities inducing a deformation of the volume enclosed between trough and crest. This deformation leads to movement and induces shear stresses at the bed. This analysis is opposite of the theoretical mechanism introduced in section 1.1, but the result is the same, and the shift

between cause and effect is simply due to different ways at looking at the process.

It is not possible to say which mechanism is the correct, since both of them appears immediately if the flow is initialized from still water.

3.4 Bed Load Transport

In this section the bed load transport will be considered. In section 3.4.1 the bed load transport capacities will be considered. In section 3.4.2 a discussion of the stability of the the ripples will be discussed.

3.4.1 Transport Capacities

The bed load capacity in the flow is defined as

$$\mathcal{C}_B = \text{sign}(U_B)\left(U_B^2 + V_B^2\right)^{3/2} \tag{3.16}$$

since it is given that without the gravity correction, $q_B \propto \theta^{3/2} \propto \mathcal{C}_B$, where U_B and V_B are the horizontal and vertical near bed velocities respectively. This quantity describes, as the name indicates, the capacity of the flow to move the sediment, in which direction the transport would go and at which phases it occur.

In the figures 3.19 and 3.20 $\mathcal{C}_B/\mathcal{C}_B^0(\mathcal{S}_1)$ is plotted for two different locations along the ripple profile, namely $x/a = 0.3$ and $x/a = 0.55$, where the former is halfway between crest and trough and the latter almost at the trough. $\mathcal{C}_B^0(\mathcal{S}_1)$ is the maximum transport capacity for the shape $\mathcal{S}_1$ on a flat bed. In the figures the color scale is limited to ± 1.5 thus large dark areas exist. This has been chosen as it is the direction and the duration of one direction or the other which is of interest and not the magnitude in itself.

In the figure 3.19 it is seen that the flow is close to periodic for almost every steepness for all of the shapes. Further it is seen that there is some protection of the motion in the trough due to the crest, thus the flow is qualitatively independent of shape and steepness as long as the curvature of the ripple crest is small. For the steepest of $\mathcal{S}_{97\%}$ the separation zone begins to come into play as seen by the negative transport capacity for $\omega t = 120°$. This tendency is even more clear in the case of $\mathcal{S}_{100\%}$, where the separation zone expands to the trough for even smaller steepnesses.

In figure 3.20 the transport capacity for the point in between the crest and the trough is depicted. It should be noted, that at this point $h \leq h_0/2$, where the equality holds for $\mathcal{S}_1$. From this is can be seen that the transport capacity is negative significantly longer than positive for even small steepnesses. This means that the transport capacity tends to give crest directed sediment transport and thus the influence of gravity is essential to give zero mean flux of bed load transport.

3.4.2 Stable Ripple Profiles

Based on the above analysis of the rigid ripple profiles, it is interesting whether or not it is possible to defined one rigid ripple profile, which is in

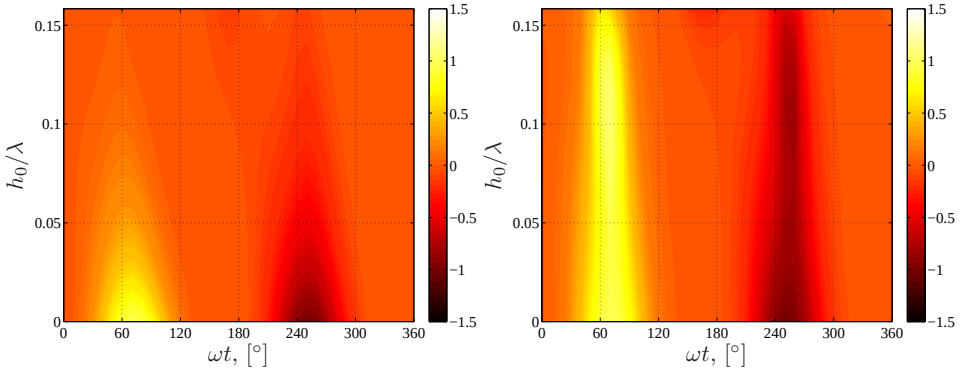

(a) Bed shape $\mathcal{S}_1$

(b) Bed shape $\mathcal{S}_2$

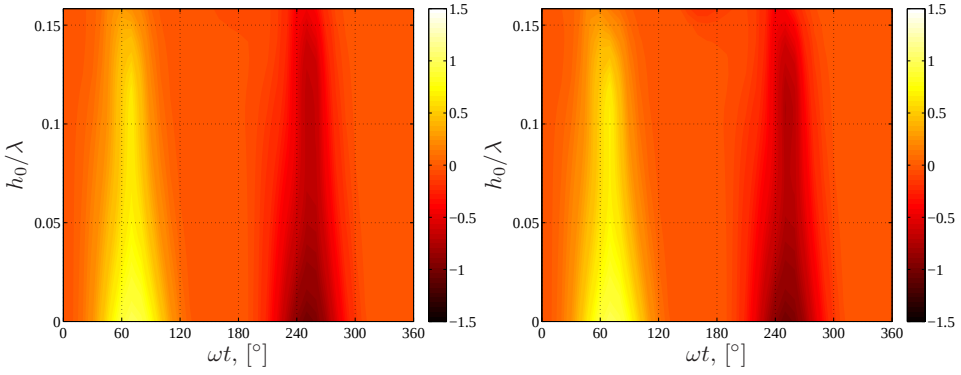

(c) Bed shape $\mathcal{S}_{91\%}$

(d) Bed shape $\mathcal{S}_{93\%}$

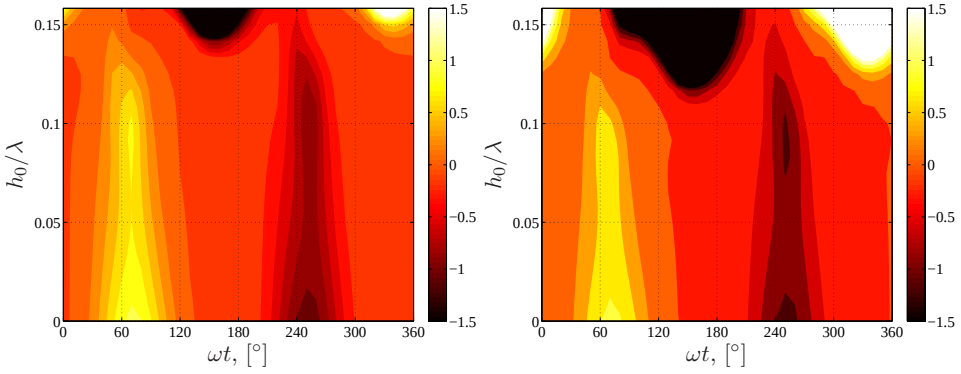

(e) Bed shape $\mathcal{S}_{97\%}$

(f) Bed shape $\mathcal{S}_{100\%}$

Figure 3.19: *The transport capacity for all six bed shapes as a function of steepness and phase in the point* $x/a = 0.55$.

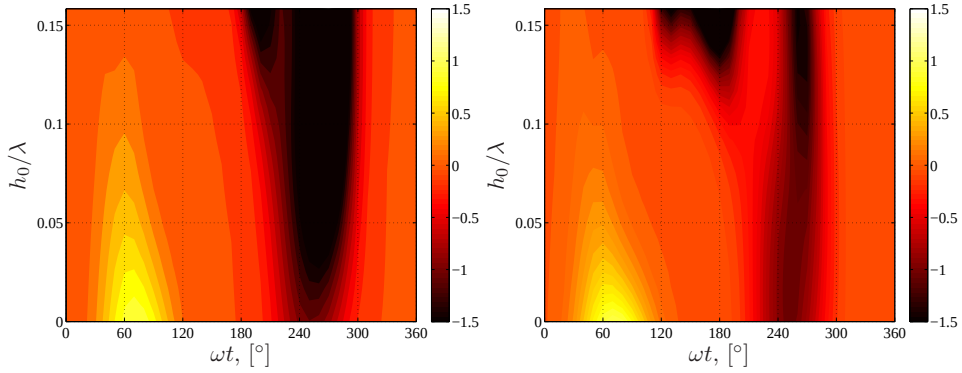

(a) Bed shape $\mathcal{S}_1$

(b) Bed shape $\mathcal{S}_2$

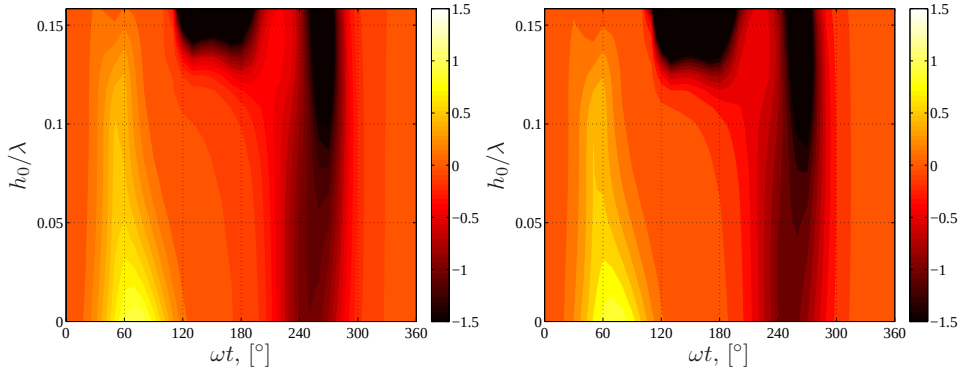

(c) Bed shape $\mathcal{S}_{91\%}$

(d) Bed shape $\mathcal{S}_{93\%}$

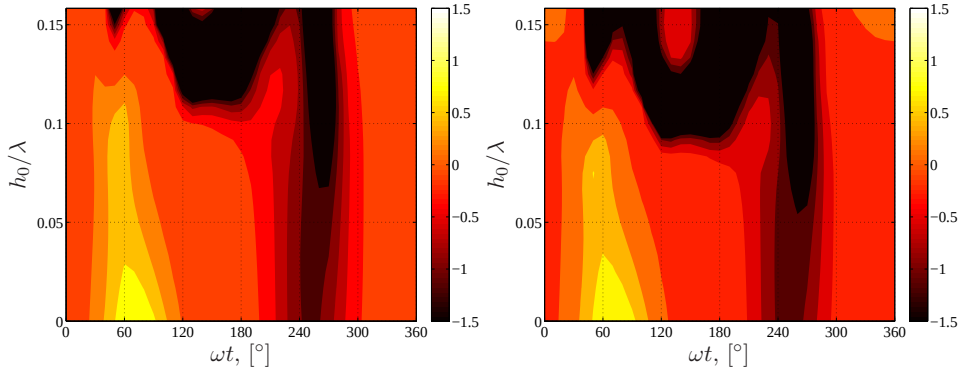

(e) Bed shape $\mathcal{S}_{97\%}$

(f) Bed shape $\mathcal{S}_{100\%}$

Figure 3.20: *The transport capacity for all six bed shapes as a function of steepness and phase in the point* $x/a = 0.30$.

equilibrium under the given conditions. Considering the ripple profile in figure 3.21, the strongest definition of stability most be

$$I_{\Phi_B} = \frac{1}{\int_0^{1/2} \|\mathbf{h}'(S)\| \mathrm{d}S} \int_0^{1/2} |\overline{\Phi}_B| \, \|\mathbf{h}'(S)\| \mathrm{d}S = 0 \quad , \tag{3.17}$$

i.e. the period averaged bed load transport is zero along half the ripple profile. This has not been achieved for any combination of the investigated profiles or test cases. Thus to give an estimate of a stable steepness as a function of shape and $\mathcal{M}$, a looser definition has to be chosen.

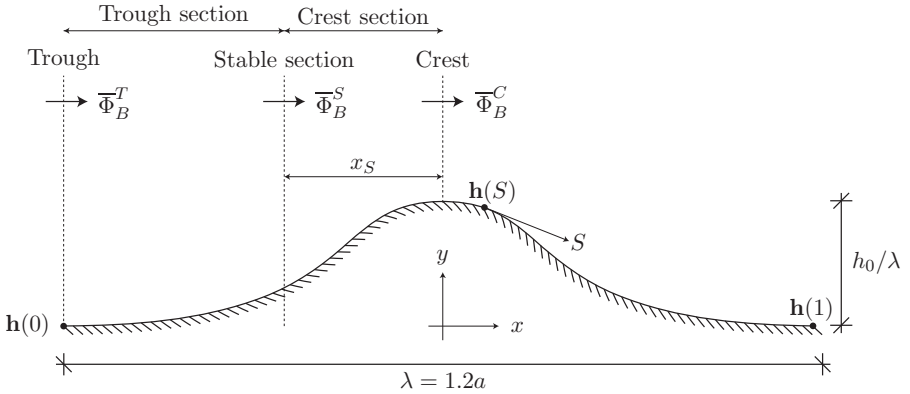

Figure 3.21: *Sketch of the considered ripple with a definition of the different quantities.*

This looser definition is indicated in figure 3.21 by the distance x_S from the crest. The stability criterion can be defined in two different ways, namely based on a magnitude consideration or a gradient consideration. These two approaches have different properties in terms of morphologically evolution of the bed shape. First the continuity equation of sediment is examined using

$$\frac{\partial h}{\partial t} = -\frac{\partial q_B}{\partial x} \tag{3.18}$$

where porosity is incorporated in q_B. This gives that the rate of change in slope using the above must be

$$\frac{\partial}{\partial t}\frac{\partial h}{\partial x} = -\frac{\partial^2 q_B}{\partial x^2} \quad . \tag{3.19}$$

With this in mind, the two approaches will be presented.

1. Having that $\overline{\Phi}_B^T$ and $\overline{\Phi}_B^C$ must be 0 due to symmetry consideration, i.e. the transport in the trough and at the crest respectively, then if

a point at the distance x_S exists such that $\overline{\Phi}_B^S = 0$, then the ripple is termed stable. The underlying argument is that having such a point, the ripple does only change locally as no transport takes place between the trough and crest sections. Looking at the equations (3.18)-(3.19) this allows the ripple profile to alter both height and slope in the stable point. Thus the stable point is given two degrees of freedom.

2. The second definition of stability restricts the degrees of freedom to one, namely demanding that $\partial \overline{q}_B / \partial x = 0$ for $x = x_S$. The underlying argument is in this case that the profile does redistribute sediment across the stable point x_S, but since the gradient of the transport is zero only the slope in the point changes due to (3.18).

Though the second leaves the stable point with fewer degrees of freedom and thus more rigidly defined, there are some problems in defining this quantity, see figure 3.22. This behaviour in $\partial \overline{h}/\partial t$ is extremely explosive and is for obvious reasons not stable if taken a morphological step. Due to this behaviour, the second approach is discarded.

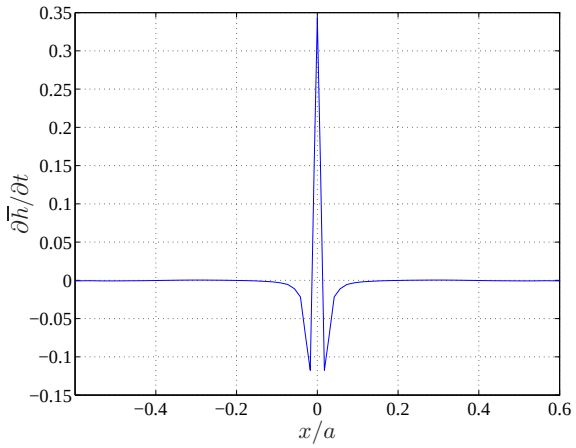

Figure 3.22: *The gradient in $\overline{q}_B$ expressed as $\partial \overline{h}/\partial t$.*

It was considered to take some value of x_S and find the combination of shape and steepness which would fulfill $\overline{q}_B = 0$. This gave scattered data, thus instead the inverse approach was adopted, namely determine x_S.

The results are given in the figures 3.23(a)-3.23(f). In these figures the value of x_S is reported, where the possible interval is [0, 0.6] with 0 being the crest and 0.6 the trough. Further the lee side phase lag, ϕ_- and the x-coordinate where $h(x) = h_0/2$ is plotted, the latter as the solid green line.

1. First of all it should be noted that even though a x_S exist it will not be regarded as a stable point, if $x_S/a > 0.3$, since it is regarded as

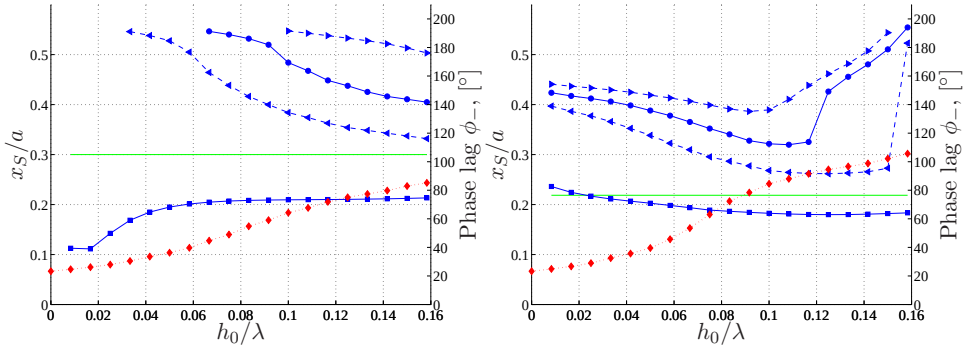

(a) Ripple shape $\mathcal{S}_1$

(b) Ripple shape $\mathcal{S}_2$

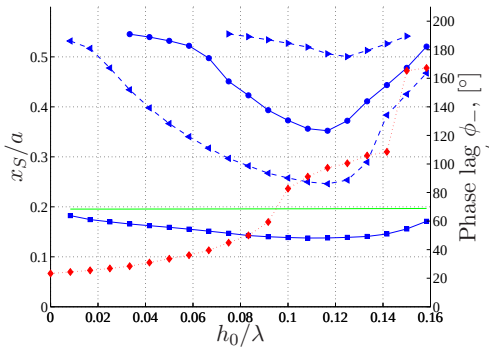

(c) Ripple shape $\mathcal{S}_{91\%}$

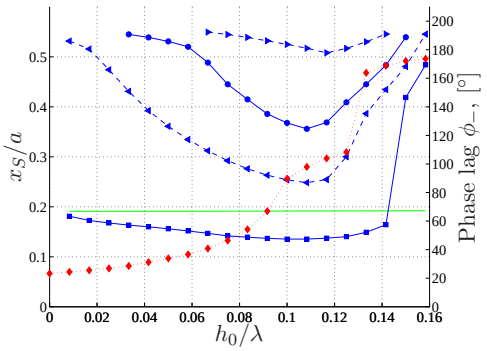

(d) Ripple shape $\mathcal{S}_{93\%}$

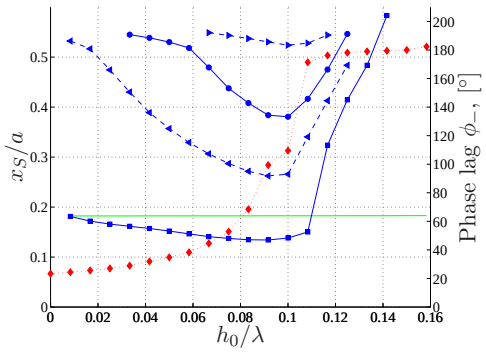

(e) Ripple shape $\mathcal{S}_{97\%}$

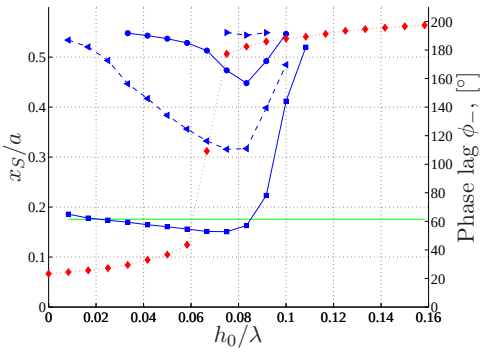

(f) Ripple shape $\mathcal{S}_{100\%}$

Figure 3.23: *Plot of the x_S/a-coordinate, where a zero period averaged bed load transport is encountered for the first time measured from the ripple crest.* ■*: Test case* **A**, $\mathcal{M} = 1.31$. ◀*: Test case* **B**, $\mathcal{M} = 2.15$. ●*: Test case* **C**, $\mathcal{M} = 2.74$. ▶*:Test case* **D**, $\mathcal{M} = 3.45$. –*: x/a-value, where $h(x/a) = h_0/2$.* ♦*: The phase lag, ϕ_-, from section 3.2.2 for test case* **D**

being so far away from the crest that everything can happen. This is further supported by the green line indicating $h(x) = h_0/2$ which is less than $0.3a$ from the crest.

2. It is noted that for smaller $\mathcal{M}$, x_S is smaller, i.e. the stable point is closer to the crest. As the bed shear stress at the crest are larger because the ripple is most exposed at that point, this is expected, as the smaller the mobility number the more exposed the sand grains can be and still be kept in equilibrium by gravity as a period averaged consideration.

3. None of the test cases **D** gives any indication of stability and hardly any of the cases **C** except for $\mathcal{S}_2$, where x_S/a tends to the upper limit 0.3.

4. Choosing the location where $h(x) = h_0/2$ to be the limiting value for x_S it is seen that the possible solutions are even more limited, actually limited to test case **A** exclusively.

5. As the phase lag increases so does x_S. The behaviour of ϕ_- and x_S is actually well correlated with a sudden increase in x_S when ϕ_- tend to become larger than 180°. Thus the slope of the ripples are simply not large enough to induce a sufficiently large retarding force from gravity. Further this supports the analysis of the transport capacities, where the crest directed capacities became large compared to the trough directed when moving up the ripple face toward the crest.

6. Considering the rounding of the crest in the case of the parabolic shapes it is seen that there are some pronounced shape similarities. The decrease and increase in x_S takes place in the same manner, and for the smoothed ones the minimum of x_S is achieved for $\phi_- = 100°$. Further it is seen that the more the crest is rounded the smaller x_S can become and more importantly, the more the ripple is smoothed the larger the number of possible solutions, e.g. there is no x_S for $\mathcal{S}_{100\%}$ at steepnesses larger than 0.11.

In figure 3.24 the stability based on two different definitions has been summerized. These definitions are $\overline{q}_B = 0$ for $x/a = 0.3$ and $\overline{q}_B = 0$ for $x = h^{-1}(h_0/2)$ respectively. This figure shows two thing, namely as already stated that it is only for $\mathcal{M} = 1.31$ and $\mathcal{M} = 2.15$ that it is possible to find a stable point. Further test case **B** dominates for the first approach and in the latter the second approach dominate. The trend though is the same, namely for increasingly sharp crested ripples the stable steepness is decreased. Further it is seen that for both approaches test case **A** and **B** have an upper and a lower solution, which with reference to ϕ_- corresponds to a rolling grain ripple and a vortex ripple respectively.

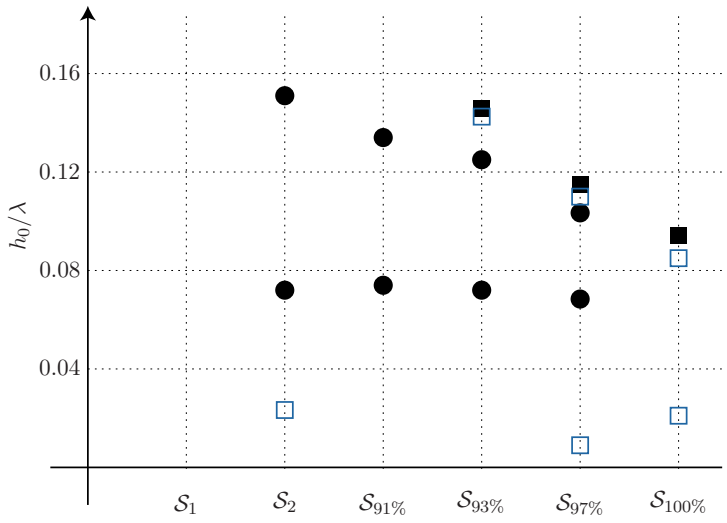

Figure 3.24: *The stable steepness as a function of shape for two different definitions of stability. Filled:* $\overline{q}_B = 0$ *for* $x/a = 0.3$. *Empty:* $\overline{q}_B = 0$ *where* $h(x) = h_0/2$, *i.e. green line in figure 3.23.*
□/■*: Test case* **A**. ○/●*: Test case* **B**

These observations results in the concluding remarks that none of the rigid ripples has been found to be stable for $\mathcal{M} > 2.15$. For very small steepnesses such a stability point does not even exist which symbolizes a pure crest directed transport, i.e. a growth of the ripple. When the steepness exceeds some value, stable points are to be found, but they are not close to the upper bound chosen for x_S. This means that non of the investigated shapes are well suited for describing the ripple shape for $\mathcal{M} > 2.15$.

For $\mathcal{M} \leq 2.15$ on the other hand stable shapes has been found and the interesting thing is that due to the U-shape of the curves in figure 3.23 it is possible to find two solutions for the different shapes, namely solutions lying in the rolling grain ripple regime and the vortex ripple regime respectively. Even though two solutions can be found, it is unlikely that the rolling-grain ripple solution will be stable, as a small perturbation on top of the ripple will increase the maximum bed shear stress and therefor an increase in the bed load toward the crest will be the consequence. Thus this procedure will not stop until the stable vortex ripple is reached.

Chapter 4

Dynamic Ripples and Morphology

In this chapter, the dynamics of ripple profiles will be discussed. This is both in terms of dynamics within one wave period due to a perturbation on top of the rigid ripple, which moves back and forth with the flow and in terms of morphological updating of the ripple profile based on period averaged quantities.

First the phase resolved dynamics of the ripple will be discussed in section 4.1. Secondly the attempts to apply morphological updating on the ripple profile will be discussed in section 4.2. The former type will be termed "dynamic ripple" in the following.

4.1 Dynamic Ripple

The dynamic ripple is based on one of the rigid ripple profiles discussed in chapter 3. On top of this rigid shape a small perturbation is placed, which is the only part of the entire ripple, which is allowed to move. The perturbation is both considered using a triangular shape, i.e. sharp, and a smooth shape.

The size of the triangle is based on the semi-period averaged quantities of the flow. The cross sections in figure 4.1 has been chosen such that $\int_0^T q_B^{A_1} \mathrm{d}t = \int_0^T q_B^{A_2} \mathrm{d}t = 0$. Hence the integral $\int_0^{T/2} q_B^{A_1} \mathrm{d}t = \int_0^{T/2} q_B^{A_2} \mathrm{d}t = C$ due to symmetry reasons.

Due to this symmetry condition there will be mass conservation inside the part of the ripple profile constrained by A_1 and A_2. Hence the volume exchanged over the crest over half a wave period from the left hand side to the right hand side can be expressed as

$$V = \frac{1}{1-n} \int_0^{T/2} q_B^C - q_B^{A_1} \mathrm{d}t \tag{4.1}$$

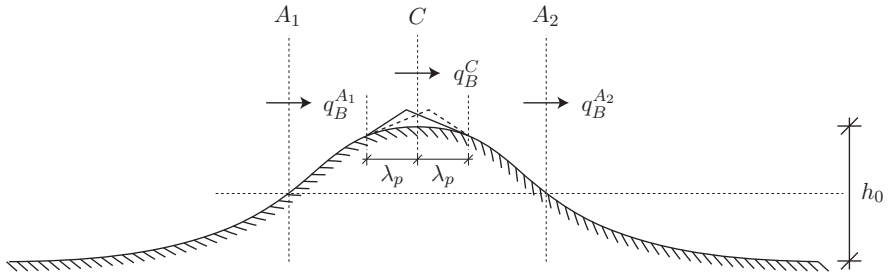

Figure 4.1: *Sketch of the entire ripple profile with a perturbation on top of the crest. The size of the perturbation is based on the sediment transport averaged over one half wave period.*

in deposited volume. This information can be used to calculate the size of the perturbation.

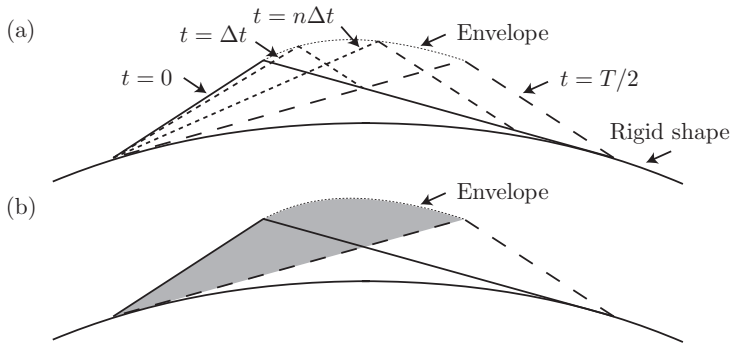

Figure 4.2: *Sketch of the dynamic perturbation on top of some rigid shape. (a) Principal movement of the perturbation profile. The time is local in terms of the near bed velocity and not the free stream velocity. (b) The shaded area is the volume moved each half period.*

In figure 4.2 the phase resolved movement of the ripple over half a wave period is sketched. At $t = 0$, the left side stands with the angle of repose and the right hand side has a more gentle slope. As this profile evolves the left side of the triangle gets an increasingly more gentle slope and the moved sand is placed at the top, so the new top slopes toward the right with the angle of repose. This process continues until $t = T/2$, where the profile is the mirror of the one at $t = 0$. The initial gentle slope is the tangent to the rigid profile. From this the maximum shape of the perturbation is limited to the hatched area in figure 4.2 being equal to V in (4.1).

In Andersen (1999), figure 6.31, it is seen that during a half wave period, it is actually the entire ripple profile which is active, and not only small movements at the crest. Since this analysis is to evaluate the effect of small

perturbations on the period averaged quantities, significant changes is not desired, thus the size of the triangle is restricted by αV, where $\alpha = \mathcal{O}(1\%)$ in the present work.

The only drawback of this formulation is that the crest becomes sharp even though a smooth rigid bed profile is used as basic shape. Thus it is hard to evaluate whether the effect is due to the movement or the sharp crest. A formulation of a smooth dynamically moving crest has not been derived due to the much more complex mathematical formulation, if the same principal as in figure 4.2 should be followed.

Instead a more simple approach has been adopted. Namely, choose some smooth perturbation and combine this with its mirrored counterpart into time independent shape functions. Expressed mathematically, this gives

$$\eta_P(t) = (1 - \beta(t))\eta_p^- + \beta(t)\eta_p^+ \tag{4.2}$$

where η_P is the time dependent perturbation and $\eta_p^\pm$ are the shape functions constant in time with the weight β being time dependent.

4.1.1 Preliminary Investigation

The preliminary investigation is to see the effect of how to move the dynamic part of the ripple. The investigation has been made with both procedures, i.e. sharp and smooth perturbations. Two methods of moving the perturbation is investigated. Both changes is based on transport of volumes of sediment. The first method is to move a constant volume per time step and the second method is to move a volume which is proportional to U_B^3 each time step. The latter as U_B^3 is proportional to the bed load transport. U_B is taken at the crest.

In figure 4.3 the period averaged bed shear stress and the period averaged bed load transport is plotted. The grid points move in space due to the change in the bed shape, but since the analysis is based on bed properties it is assumed that a direct averaging can be applied with no consideration to the movement of the bed.

As seen from the results there is two main conclusions which can be derived from this preliminary investigation. First of all the maximum in the period averaged bed shear stress become smaller if the perturbation is moved with a velocity proportional to the crest velocity. This is reasonable, otherwise the perturbation will move to fast around flow reversal and to slow during occurrence of the maximum outer velocity, i.e. inducing a local and non-physical velocity field. Secondly, it is seen that the sharp crested method gives rise to global changes, which must be due to the more well defined separation point due to the sharp crest. In the case of smooth perturbation on the other hand, there is practically no influence on the properties away from the crest.

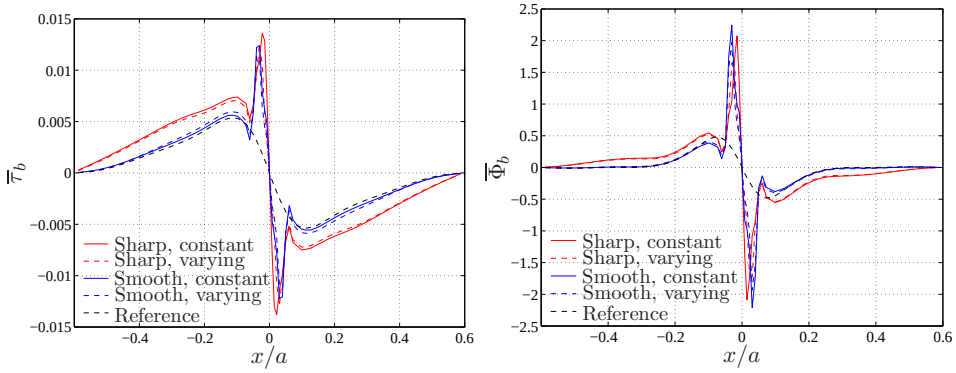

(a) $\overline{\tau}_b$ over dynamic ripple

(b) $\overline{\Phi}_B$ over dynamic ripple

Figure 4.3: *The effect on $\overline{\tau}_b$ and $\overline{\Phi}_B$ due to a dynamically moving ripple crest. Sharp is the sharp crested method, smooth the smooth crested, constant is constant movement of the perturbation and varying is movement based on U_b^3. The reference bed shape is $\mathcal{S}_2$ with $h_0/\lambda = 0.117$.*

It is seen that both types of perturbations give rise to a significant increase in the bed shear stress and bed load transport. But only the triangular shaped perturbation gives rise to a global effect, i.e. away from the ripple crest. The significant peaks in both the bed shear stress and the transport can originate from either the additional slope on top of the otherwise flat ripple, i.e. increased convective acceleration, or it could also be that the discretization of the perturbation is not sufficiently fine, as only a few points describes the crest.

4.1.2 Results with Perturbed Ripples

Based on this preliminary investigation it is decided that the movement of the bed should follow the velocity at the crest and due to the uncertainty of the effect of the discretization, $\mathcal{N}_x = 80$ is chosen. The rigid shape will be $\mathcal{S}_{91\%}$ and analysed for all steepnesses. The triangular perturbation is defined such that the effective height of the ripple is increased by 7.5%. The smooth perturbation is defined as a smoothing of the triangular shape.

The bed is updated 360 times per wave period and $\mathcal{N}_T = 3600$.

Two different results have been extracted from these data sets. These are the amplification factor and the value of x_S/a, i.e. the distance from the crest to the point where $\overline{\Phi}_B = 0$. These results can be seen in figure 4.4(a) and 4.4(b) respectively. In these, reference data from the two ripple profiles $\mathcal{S}_{91\%}$ and $\mathcal{S}_{100\%}$ are also presented. In should be noted that not all the results are fully converged, i.e. $\Delta Q > \Delta Q_0$ and this is presented with

empty markers on the lines.

From these results, two main conclusions are derived, namely inducing a perturbation on top of a ripple greatly increases the maximum bed shear stress, actually the amplification factor in the case of the sharp perturbation is even larger than for $\mathcal{S}_{100\%}$ even though the effective steepness is smaller.

Further the stability is greatly disturbed and both types of perturbations tends to the stability shape of $\mathcal{S}_{100\%}$ even though the perturbations are on top of $\mathcal{S}_{91\%}$. The perturbed solutions have quantitatively more in common with $\mathcal{S}_{100\%}$ than $\mathcal{S}_{91\%}$. This further shows that the actual shape of the ripple crest is of paramount importance for the flow characteristics and sediment transport patterns.

4.2 Morphology

Different attempts to update the bed to achieve a morphological development to obtain a bed shape, which fulfill the stability condition given by equation (3.17), has been tried. Though none have been successful, a short overview of the attempts and the drawbacks will be given here.

1. An integrated approach was the first attempt, where one or two points in between the ripple trough and crest was chosen. Based on the period averaged bed load transport over these points, the bed shape over the entire ripple profile was updated. This was tried with and without mass conservation of the sediment.

   The drawbacks in this approach was that the flow is extremely sensitive to the shape of the ripple and especially the behaviour of the crest, thus to give a good description of the shape in between the considered points was not found to be an easy task without any knowledge of the sediment transport in between these points.

2. Therefor a full morphological updating procedure was considered using equation (3.18) in every point along the ripple.

   The drawbacks in this approach was that the resulting $\partial\overline{h}/\partial t$ terms had some extreme peaks at the crest, see e.g. figure 4.5, which it was not possible to smooth using any of the ordinary smoothing routines. Peaks of that kind resulted in extremely small morphological time steps when updating the bed, and further a more pronounced peak appeared. A peak which in the previous analysis is seen to increase the amplification factor and hence the sediment transport toward the crest. Further due to the sign change at the crest in $\partial\overline{h}/\partial t$, the bed shape after a few iterations revealed a triple peaked ripple. This happened typically significantly before the slope exceeded the angle of repose.

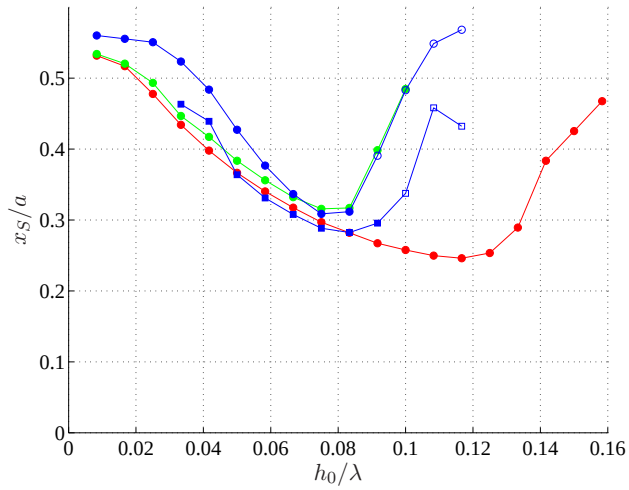

(a) x_S/a for different perturbations

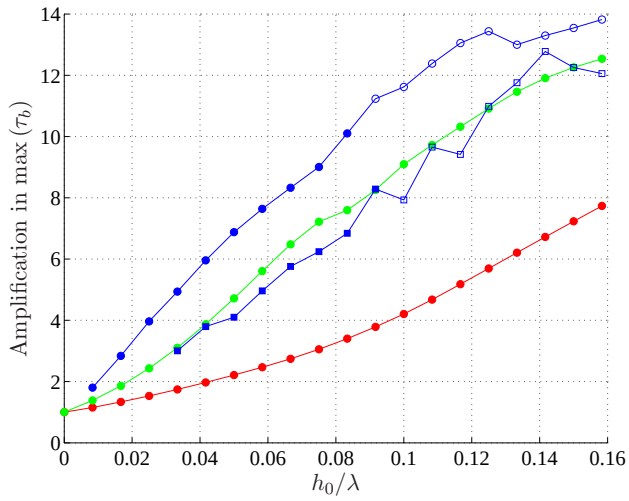

(b) Amplification factor for different perturbations

Figure 4.4: *The value of x_S/a and the amplification factor for both sharp and smooth perturbations on top of $\mathcal{S}_{91\%}$. Red: Reference for $\mathcal{S}_{91\%}$. Green: Reference for $\mathcal{S}_{100\%}$. ■: Smooth perturbation. ●: Sharp perturbation. Filled: Converged. Empty: Non converged.*

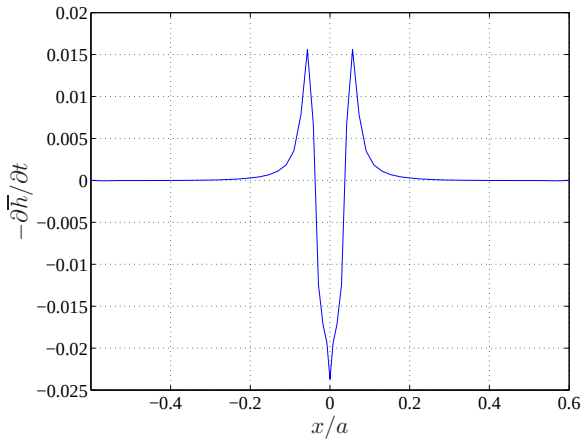

Figure 4.5: *The morphological change, $\partial\overline{h}/\partial t$, based on the gradient in $\overline{q}_B$ for test case* **B** *over $\mathcal{S}_{91\%}$ with a steepness of 0.117.*

The failure in achieving a full morphological evolution of the ripple profile might also be due to the clustering of the points at the crest. In figure 4.6, $\partial\overline{h}/\partial t$ for $\mathcal{S}_1$ with the steepness $h_0/\lambda = 0.15$ has been plotted for both a clustered point distribution and an equidistant point distribution. As can be seen, using the equidistant point distribution, the peak in $\partial\overline{h}/\partial t$ disappears. This would allow for a much more robust updating in a morphological scheme. The discouraging result is that the removal of the peak has only been successful over $\mathcal{S}_1$ whereas it does not disappear on an equidistant grid on $\mathcal{S}_2$ which is the second most smooth profile.

Further it should be noted that there is no influence from the point distribution just a little distance from the crest.

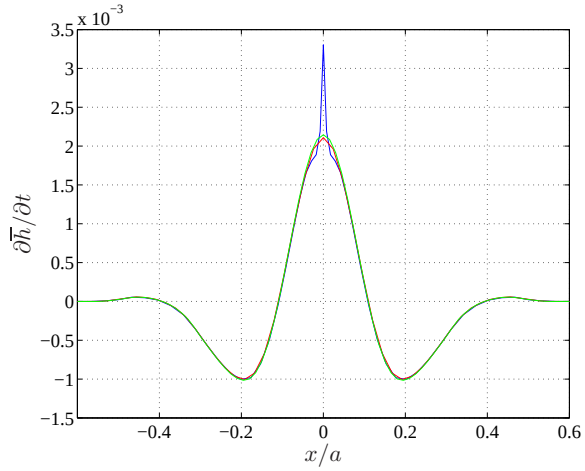

Figure 4.6: *The difference in* $\partial\overline{h}/\partial t$ *for clustered and equidistant distribution of the points along the bed. Blue: Clustered,* $\mathcal{N}_x = 50$*. Red: Equidistant,* $\mathcal{N}_x = 50$*. Green: Equidistant,* $\mathcal{N}_x = 80$*.*

Chapter 5

Discussion and Future Work

In this chapter the main results presented in chapters 3 and 4 will be discussed. Further a short section will describe the issues which it would be interesting to address in future works.

5.1 Discussion

In chapter 3 a thorough presentation of the numerical results was given. These results show a flow pattern which increases in intensity with increasing sharpness of the ripple. The flow quantities was the strength of the recirculation zone, Γ_0, the ripple averaged bed shear stress, I_τ, and the phase lag between flow separation on the lee side of the ripple and the free stream flow. Further there was found a significant increase in the maximum bed shear stress as a function of increasing curvature of the ripple crest.

Based on these informations together with the bed load transport, it is obvious to draw the conclusion that ripple profiles with a large curvature of the crest will be hard to get stable, since the extreme magnitude of the Shields parameter in this work would directly give a rounding of the crest, thus it cannot be stable. This is further supported by theoretical considerations.

In Fredsøe and Hedegaard (1983) the argument which lead to the parabolic ripple profile involves a discontinuity in the bed shear stress at the crest. This discontinuity relates to $\partial\overline{h}/\partial x$ thus giving a discontinuity in the slope. What on the other hand is expected is that the top of the ripple moves back and forth, as noted by both Sleath (1984) and in the numerical investigation by Andersen (1999). Thus the period averaged bed shear stress is expected to be smoothed to yield a continuous distribution along the ripple profile, and thus the ripple profile cannot contain a discontinuity in the slope, i.e. the profile must be expected to be smoothed to some degree.

The smoothing through a dynamic perturbation was investigated, but the exact opposite was found, namely that the bed shear stresses are in-

creased and the stability limit, defined by x_S/a, is almost vanishing. This investigation shows that the shape of the crest and dynamic behaviour is of paramount importance for the flow description. Even that of choosing a smooth perturbation instead of a sharp lead to significant differences. The most significant change is that the sharp crested ripple gives global impact where as the smooth only influences the near crest area.

The actual shape of the perturbation can also be discussed, as the present formulation is a minor movement of sediment directly on top of the crest. This does not support the findings that the semi-period averaged sediment transport over the crest is $\mathcal{O}(100)$ times larger than the volume of sediment moved in the present formulation. This support the sketch in Sleath (1984), see reproduction in figure 5.1, that the dynamic part of the ripple is placed on the side of the ripple slope and not on the crest. The actual mechanism in moving the sediment from one side to the other is not discussed, but one theory could be, that large Shields parameters at the crest gives almost no gradient in Φ_B thus all the sediment is simply transported over the crest and deposited on the lee side of the ripple. This theory should further include the finding that the smooth ripple profile has attached flow on part of the lee side. To a first extend it can be estimated that the drop in bed shear stress on the lee side is sufficiently large to deposit most of the sediment close to the crest.

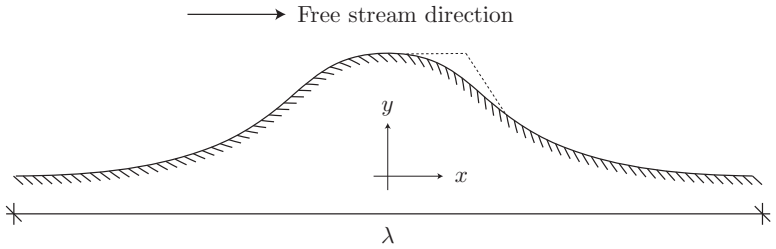

Figure 5.1: *Reproduction of figure 4.7 in Sleath (1984) showing the phase resolved movement of the ripple crest.*

Though the parabolic profile with a small rounding is disregarded as a possible equilibrium profile in the present analysis, it is not utterly impossible. It is not impossible since the case of subcritical Shields parameters on a flat bed has not been investigated. This would lead to supercritical Shields numbers on a perturbed bed, but the increase would not come near the sheet flow state. But it should be emphasized that it is not $\mathcal{S}_{100\%}$ which is thought of, but one of the smoothed parabolic shapes.

It was further seen that the increase in the phase lag, ϕ_-, gave rise to significant crest directed transport capacities simply because of the increase in the period averaged bed shear stress over half the ripple length, I_τ. Further it was seen that none of the bed shapes with $\mathcal{M} > 2.15$ could

be termed stable. This can only be explained by the amplification factors in the bed shear stress, thus the sediment transport at the crest would be in a state of sheet flow for some period of time. This means that suspended sediment transport cannot be disregarded as a mechanism of redistributing the sediment away form the crest for large $\mathcal{M}$.

The amplification factor further explains why no solutions for a stable ripple exist at all for $\mathcal{S}_{97\%}$ and $\mathcal{S}_{100\%}$ if the steepness becomes to large. For these steepnesses the amplification factor and the phase lag corporate to make the near bed flow crest directed and inducing large shear stresses, thus the gravity correction to the Shields parameter is insignificant.

When comparing all the results from the flow analysis it is seen that for small steepnesses there is minor shape dependence, but increasing the steepness pronounced differences occur. The key point is that the smooth ripples cannot achieve the same magnitudes in say strength, bed shear stress, etc, even though the smooth ripples are increased in steepness. This shows that for large steepnesses it is essential to know the actual shape of the ripple to describe the flow accurately. As a consequence, having a co-existing current, the net-sediment transport is extremely dependent on the actual shape of the ripples, as the correlation between bed shear stress and ripple shape is not expected to be significantly different in that case.

One comment should be given the amplification factor and the bed shear stresses in general. It is seen that the bed shear stresses in general are larger in the case of steep parabolic ripples than for the cosine ripple. The actual distance from the bed to the first computational cell in terms of wall coordinates is smaller for the cosine ripple than the parabolic ripples, as the friction velocity is smaller. Thus the prediction of the shear stresses over the cosine bed is better than for the parabolic. This leads to a smaller difference in the amplification factor than there actually is, but it is only a matter of few percent, thus probably not of any significance.

5.2 Future Works

One of the key obstacles using the present code has been the slow convergence rate for certain configurations. Some flows did not even converge to a solution with $\Delta Q < \Delta Q_0$ in 10.000 wave period. This is clearly not acceptable, thus a more stable algorithm for making the solution convergence is necessary.

Further, suspended sediment has been mentioned in the previous chapters, thus an obvious step is to include suspended sediment in the calculations and see what the effect on stability will be.

Finally, studies comprising of combined waves and current should be undertaken, as this combination are closer to realistic conditions than the conditions investigated in the present work.

Chapter 6

Conclusion

In this work the flow and bed load transport over ripples under the influence of oscillatory flow has been investigated using a numerical model.

There has been made a parametric study where the ripple shape, the ripple steepness and the flat bed Shields parameter have been varied.

With respect to the flow, it is seen that increasing the steepness of the ripples gives rise to a contraction of the flow, which results in an increase in the maximum bed shear stress compared to the one induced on a flat bed. This amplification is seen to vary with the actual ripple profile. For large curvatures of the bed shape an amplification factor up to 12 is achieved. For more gently changing bed shapes the amplification factor does not exceed 4.

Due to the presence of a ripple, a non-zero period averaged bed shear stress is seen and this is further seen to vary with the shape and steepness in the same manner as the amplification factor. This non-zero bed shear stress is found to drive a recirculation zone and the extend of this recirculation into the main flow has been mapped. This mechanism is important for suspended sediment transport.

With respect to the bed load transport the dependence on the amplification is clearly seen, as the sharp crested ripples achieves large Shields numbers at the crest; so large that it is unlikely that the sharp crested (or even ripple shapes with large but finite curvature at the crest) can be stable as a period averaged consideration as the crest will be smoothed due to the large bed shear stresses.

The amplification factor has been investigated in further detail, namely the dependence of this quantity on the behaviour of the crest. This is done by perturbing the rigid ripple profile with a dynamic part, which moves back and forth. This perturbation lead to significantly increased amplification factors, but the way to perturbed the ripple was questioned.

Finally it should be stressed that it is not sufficient to map the ripples by such quantities as the ripple height, h_0, the ripple length, λ, the Shields

parameter, θ, and the free stream quantities. In this work it is seen that the shape is essential for the flow and sediment transport.

Bibliography

Andersen, K. H. (1999). *The Dynamics of Ripples Beneath Surface Waves and Topics in Shell Models of Turbulence*. Ph.D. thesis, Centre for Chaos and Turbulences Studies, The Niels Bohr Institute, University of Copenhagen.

Bagnold, R. (1946). Motion of waves in shallow water. interaction between waves and sand bottoms. *Proceedings of the Royal Society of London. Series A, Mathematical and Physical Sciences*, **187**(1008), 1–18.

Dixen, M., HAtipoglu, F., Sumer, B. M., and Fredsøe, J. (In print, 2007). Wave boundary layer over a stone-covered bed. *Coastal Engineering*.

Engelund, F. and Fredsøe, J. (1974). *Transition from Dunes to Plane Bed in Alluvial Channels*. 4. ISVA, Technical University of Denmark.

Fredsøe, J. (1974). On the development of dunes in erodible channels. *Journal of Fluid Mechanics*, **64**, 1–16.

Fredsøe, J. and Deigaard, R. (1995). *Mechanics of Coastal Sediment Transport*, volume 3 of *Advanced Series on Ocean Engineering*. World Scientific, 1st edition.

Fredsøe, J. and Hedegaard, I. B. (1983). Shape of oscillatory sand ripples. *Progress Report*, (58), 19–29.

Fredsøe, J., Andersen, K. H., and Sumer, B. M. (1999). Wave plus current over a ripple-covered bed. *Coastal Engineering*, pages 177–221.

Gray, C., Fredsøe, J., and Deigaard, R. (1991). Flume experiments on bed wave shape and sand transport by currents and waves. *Progress Report*, (73), 7–20.

Hedegaard, I. B. (1985). *Wave Generated Ripples and Resulting Sediment Transport in Waves*. Ph.D. thesis, Technical University of Denmark.

Jensen, B. L., Sumer, B. M., and Fredsøe, J. (1989). Turbulent oscillatory boundary layer at high reynolds numbers. *Journal of Fluid Mechanics*, **206**, 265–297.

Patel, V. C. and Yoon, J. Y. (1995). Application of turbulence models to seperated flow over rough surfaces. *Journal of Fluids Engineering*, **117**, 235–241.

Sleath, J. F. A. (1984). *Sea Bed Mechanics*. John Wiley & Sons.

Sumer, B. M., Chua, L. H. C., Cheng, N.-S., and Fredsøe, J. (2003). Influenceof turbulence on bed load sediment transport. *Journal of Hydraulic Engineering*, pages 585–596.

Tjerry, S. (1995). *Morphological Calculation of Dunes in Alluvial Rivers*. Ph.D. thesis, Institute of Hydrodynamic and Hydraulic Engineering, Technical University of Denmark.

Wilcox, D. C. (1993). Comparison of two-equation turbulence models for boundary layers with pressure gradient. *AIAA Journal*, **31**(8), 1414–1421.

Wilcox, D. C. (1994). *Turbulence Modeling in CFD*. DCW Industries, Inc., 1st edition.

Wilcox, D. C. (2006). *Turbulence Modeling in CFD*. DCW Industries, Inc., 3rd edition.